

Nanoindentation of virus capsids in a molecular model

Marek Cieplak¹ and Mark O. Robbins²

*¹Institute of Physics,
Polish Academy of Sciences,
Aleja Lotników 32/46,
02-668 Warsaw, Poland*

*²Department of Physics and Astronomy,
Johns Hopkins University,
3400 North Charles Street
Baltimore, MD 21218, USA*

Abstract

A molecular-level model is used to study the mechanical response of empty cowpea chlorotic mottle virus (CCMV) and cowpea mosaic virus (CPMV) capsids. The model is based on the native structure of the proteins that constitute the capsids and is described in terms of the C α atoms. Nanoindentation by a large tip is modeled as compression between parallel plates. Plots of the compressive force versus plate separation for CCMV are qualitatively consistent with continuum models and experiments, showing an elastic region followed by an irreversible drop in force. The mechanical response of CPMV has not been studied, but the molecular model predicts an order of magnitude higher stiffness and a much shorter elastic region than for CCMV. These large changes result from small structural changes that increase the number of bonds by only 30% and would be difficult to capture in continuum models. Direct comparison of local deformations in continuum and molecular models of CCMV shows that the molecular model undergoes a gradual symmetry breaking rotation and accommodates more strain near the walls than the continuum model. The irreversible drop in force at small separations is associated with rupturing nearly all of the bonds between capsid proteins in the molecular model while a buckling transition is observed in continuum models.

INTRODUCTION

Understanding the properties of self-assembled molecular structures such as virus capsids is of great current interest. Capsids are conglomerates of proteins that protect virus's genomes. They are generally strong mechanically, especially when they envelope tightly packed DNA at high internal pressures. For instance, in bacteriophage $\phi 29$, the pressure is of order 50 atm [1–3]. Capsids that protect single stranded RNA have an order of magnitude lower pressures, as evidenced by Michel et al. [5] for the cowpea chlorotic mottle virus (CCMV), but they are still quite sturdy.

One way of assessing the elastic properties of capsids is by making nanoindentation measurements with an atomic force microscope. In particular, it has been found [5] that the CCMV capsids with their RNA removed resist nanoindentation less (by about 30%) than their full counterparts. Both types of CCMV capsids are highly elastic – the initial Hookean reversible regime persists up to nanoindentations varying between 20% and 30% of the diameter and applied forces of 600 pN and 1000 pN for the empty and full capsids respectively [5, 6]. These forces are noticeably larger than characteristic forces needed for a mechanical unraveling of proteins. As an example, titin, which is a reasonably strong protein, requires a force of about 204 pN [7, 8] to unravel whereas the particularly strong scaffoldin protein c7A requires a force of about 480 pN [9].

The sturdiness of the capsids comes from both the mechanical properties of the individual proteins and the way the proteins are bound together. Capsids have a variety of shapes and sizes, but most have highly symmetric icosahedral structures. Early models treated the capsid as a homogeneous spherical shell, first in the thin shell limit [4, 5] and then including the finite width of the shell and nonlinear response [11]. The latter work showed that a Hookean model for finite width shells did not reproduce the linear force displacement curve observed in experiments, while standard nonlinear models for rubberlike materials did give a linear response. The icosahedral symmetry of viruses has been included in the thin shell limit [2, 3, 6, 10] and using the mass density to determine a spatially varying shell thickness [12], but with homogeneous elastic response.

Many of the above models are roughly consistent with experimental behavior. The force rises linearly with displacement for an extended range and then drops suddenly, signaling an instability. The linear region can be fit by assuming elastic moduli with a reasonable

magnitude, but the fact that different models can achieve this suggests that the result is not sensitive to variations in local moduli and density that may be present in capsids. For example, one may expect that the number and geometry of bonds within proteins are different than those between proteins, and this heterogeneity is difficult to capture in continuum theories. Another issue is that the instability at higher forces in continuum models is associated with a buckling instability without any breaking of molecular bonds. The latter may be important in real capsids, but is difficult to parameterize in continuum models. More detailed models are needed to assess potential variations in elastic properties within the shell and the potential role of bond breaking.

All-atom simulations are an appealing alternative, but are limited to relatively short indentation times of order 1ns compared to experimental times of 10ms or more. Studies of mechanical properties have included an all-atom analysis of the low frequency vibrations in the satellite tobacco necrosis virus [13] and an elastic network model analysis of eigenmodes in CCMV [14] and HK97 viruses [15, 16]. Recent simulations by Zink and Grubmuller [17] have examined indentation of the southern bean mosaic capsid using an atomistic treatment with surrounding water. The force on a small ($\sim 1\text{nm}$) sphere representing the tip was measured as a function of the distance from the center of mass. They find a rather short elastic region ($\sim 1\text{nm}$) followed by a rapid drop in force. The instability is associated with bond breaking, but the bonds rapidly reform as the sphere passes through the capsid wall and into the interior. This indicates the potential importance of factors that are not included in continuum models. Both the yield elastic stiffness and yield stress are about an order of magnitude higher than experiment, but vary logarithmically with rate. The yield stress often varies logarithmically with rate in thermally activated systems [18], but it is unusual to find this variation in the stiffness. This suggests that the simulation rates are higher than the structural relaxation rate of the virus and that new behavior may occur at lower velocities.

In this paper we consider a model that is less computationally intensive, but includes coarse-grained structural information. The model is used to explore the effect of molecular structure on nanoindentation of CCMV and cowpea mosaic virus (CPMV), whose symmetry is that of a rhombic tricontahedron [22, 23]. Capsids in both systems contain of order 300 000 heavy atoms, which makes it difficult to study large mechanically-induced conformational changes with all-atom simulations. Instead we use structure-based coarse-grained molecular

dynamics models that take the experimentally determined native structure as an input to derive the effective Hamiltonian in a phenomenological way. Our implementation builds on the detailed description presented in refs. [19–21] and this approach has been successful in describing both folding and mechanically-induced unfolding of individual proteins [19, 21]. The coarse-graining reduces the number of effective protein atoms by an order of magnitude. Treating solvent molecules implicitly through random force and damping terms leads to even greater economies by eliminating atoms and increasing the effective time step.

We find that the mechanical response of the molecular model of CCMV is qualitatively consistent with experiments and continuum calculations, with a long elastic region followed by a sudden drop in force. CCMV and CPMV have similar radii, widths and densities and thus would be expected to have similar responses in continuum models. In contrast, the coarse-grained model predicts that CPMV is an order of magnitude stiffer and breaks at a higher force and smaller displacement. These large changes in mechanical response result from small changes in bonding, suggesting that the mechanical response of virus capsids may be highly variable. Experiments on CPMV would provide a test of this prediction.

The local deformations in the molecular and continuum models [12] for CCMV are compared directly. One significant difference is that the molecular model undergoes a gradual and reversible rotation in the elastic region. More strain is also accommodated near the walls in the molecular model. Dramatic differences between the models are observed at the end of the elastic region where the response becomes irreversible. In the continuum model, nonlinearities are associated with buckling. In the molecular model, nearly all of the inter-protein bonds break at the end of the elastic region. This breaking transition appears to be thermally activated and its location depends on trajectory. The mean force and displacement at rupture decrease with decreasing deformation rate, because there is more time for thermal activation.

THE MODEL SYSTEMS

CCMV is a member of the bromovirus group of the *Bromoviridae* family. It consists of a single-stranded RNA molecule encapsulated by a 180-protein icosahedral capsid. The native CCMV capsid is stable around pH 5.0, where it is characterized by the outer and inner diameters of 286 and 195 Å respectively [24]. At pH 7.0 and low ionic strength,

the capsid adopts its swollen form in which its linear sizes are increased by about 10 %. Nanoindentation studies at pH 5 yield a spring constant of about 0.15 N/m [5, 6]. At pH 6, which is half-way to the situation in which the swollen form arises, the spring constant falls by about a factor of about 3 compared to the native form [6]. Furthermore, there is no longer a sudden drop in force that would indicate mechanical instability.

The symmetries of the native capsid are those of the fullerene C_{60} . The proteins form a closed shell that has the symmetry of a truncated icosahedron comprised of 32 faces (making 90 edges and 60 vertices). 12 of these faces are pentagons and 20 are hexagons. A pentagon consists of five icosahedral asymmetric units ('kites') and a hexagon contains six such units. Molecularly, a pentagon corresponds to a pentamer and a hexagon to a hexamer. There are thus altogether 180 units, each containing a single molecule referred to as a chain. Even though the chains are sequentially identical, one distinguishes three kinds of chains: A, B, and C. The pentamers contain only the A-type chains whereas the hexamers have three chains of type B and three chains of type C. All chains contain 190 amino acids in a β -barrel fold, but their conformations have not been determined fully through X-ray crystallography. In particular, the locations of the first 41 amino acids in chain A and the first 26 in B and C are not known. These undetermined segments of the proteins are presumably in more random or mobile regions that do not contribute to the scattering or structural integrity. In our model, we make use only of the known parts of the structure and the whole capsid is represented by 28620 C^α atoms [24, 25].

The conformation of the swollen form of CCMV at pH 7 has been determined through cryo-electron microscopy [24], but at a much poorer resolution than the structure at pH 5. The resolution is comparable to the separation between C^α atoms that defines the structure in our coarse-grained model. We constructed a model based on this structure, but found that it was not mechanically stable even at $T = 0$. This could imply that atoms that are misplaced or missing from the structure are crucial to stability. Note that the virus disassembles at slightly higher pH and may be nearly unstable at pH 7. We are not aware of indentation experiments at pH 7. Given the large reduction in measured stiffness between pH 5 and pH 6 [6] and the fact that swelling of the structure mainly occurs above pH 6, it would be interesting to extend the experiments to the fully swollen regime. Structural information at pH 6 would also allow us to compare our model to experiments in the partially swollen state.

CPMV belongs to the picornavirus superfamily and can be represented by a rhombic triacontahedron with 30 rhombic faces that make 60 edges and 32 vertices [22, 23]. The capsid is assembled from two viral proteins – subunits S and L – which form three β -sandwich domains, A, B, and C in an asymmetric unit. They contain 189, 187, and 182 amino acids respectively. Domains B and C form hexamers and each L subunit comprises B- and C-type domains. The A-domains form pentamers. Altogether, CPMV contains 60 units corresponding to the total of 33 480 C^α atoms. In contrast to CCMV, the positions of all amino acids are determined.

The angle-averaged radial distributions of the C^α atoms in the two capsids in their native states are shown in Figure 1. The average radial position is 119.6 Å in CCMV and 124.3 Å in CPMV. The distributions of radii are also comparable, with total widths of about 55 Å and rms variations of 11.13 Å and 10.54 Å, respectively. In continuum theory the stiffness associated with compressing a thin shell scales as h^2/R where h is the thickness and R the radius [5]. Given the similarities in the number and radial distribution of C^α atoms one would expect similar stiffnesses, but we will see that this is not the case.

The coarse-grained models of the capsids generalize our previous approach for large conformational changes in single proteins [19–21]. We take the native coordinates of all heavy atoms in all capsid proteins from the structure files and assign van der Waals spheres to the atoms (enlarged by a factor that takes into account attraction [26]). If the spheres belonging to amino acid i , as counted along the "global" sequence, overlap the spheres related to amino acid j then we declare existence of a native contact between amino acids i and j . Most of the native contacts are between acids in the same protein, but there are also contacts that link separate proteins. Contacts corresponding to the $i, i+2$ interaction within a protein are discarded [27] as they usually correspond to dispersive interactions which are much weaker than the hydrogen bonds. Altogether, there are 62 426 native contacts in the model CCMV and 90 420 contacts in the model CPMV. This 45% increase is much greater than the change in the number of C^α atoms or their radial distribution, and may be an important factor in explaining why we find a much greater stiffness for CPMV than CCMV.

The interactions between amino acids that form native contacts are described by the Lennard-Jones (LJ) potential $V(r) = 4 \epsilon [(\frac{\sigma_{ij}}{r_{ij}})^{12} - (\frac{\sigma_{ij}}{r_{ij}})^6]$, where r_{ij} is the distance between the C^α 's in amino acids i and j , and σ_{ij} is determined for each pair to ensure that the potential minimum coincides with the experimentally measured native distance. The binding

energy parameter ϵ can be determined by comparing theoretical and experimental data for stretching of single proteins [27]. Our latest estimate [28] is that ϵ is of order 110 pNÅ (see also ref. [29]). Interactions along the backbone of each protein are described with a harmonic potential with spring constant $50\epsilon/\text{Å}^2$. This is almost an order of magnitude stiffer than the LJ interaction and ensures that the backbone bonds do not break.

The interactions between atoms that do not form native contacts are represented by a purely repulsive potential obtained by truncating the Lennard-Jones potential at its minimum at 4 Å. The potential number of non-native contacts is of order 5×10^8 . To avoid calculating all these separations at each step, we make a Verlet list [30]. The list comprises all C^α atoms that are less than 12 Å apart from another C^α atom and is made every 2000 time steps.

Langevin noise and damping terms are introduced to provide an implicit solvent [31]. The amplitude of the noise is determined by the temperature, T . All simulations described below were done at $k_B T = 0.3\epsilon$, where k_B is the Boltzmann constant. Estimates of ϵ for our model place $k_B T/\epsilon$ between 0.3 and 0.4 at room temperature. We find similar behavior for indentation over this range of temperatures although there are small changes in quantitative values. The model is simulated in the overdamped limit and the characteristic time scale τ is set by the damping rate $2m/\tau$ in the Langevin thermostat, where m is the average mass of an amino acid. For proteins in water τ is of order 1 ns as argued in refs. [32, 33]. The time step used to integrate the equations of motion with a fifth order predictor-corrector algorithm [30] is $\tau/200$.

Nanoindentation is implemented by placing the capsid between two repulsive parallel plates. This geometry corresponds to the limit of a tip with large radius and has been considered in continuum calculations. The experimental geometry is often a flat substrate with a tip whose radius is of the same order as the virus, but continuum results show that this has little effect on the stiffness. The plate potential scales as h^{-10} [34], where h is the separation between the plate and an amino acid. In the initial state, the plates are far enough apart that they do not interact with the capsid. The plates are then brought together by increasing the speed of both plates symmetrically to a value v_p over 2000 τ . In most cases $v_p = 0.0025 \text{ Å}/\tau$ giving a combined speed of $0.005 \text{ Å}/\tau$ that was found to be slow enough to produce quasistatic results in studies of protein stretching [21, 27]. We will also present results at twice this velocity and half this velocity and refer to these as fast and slow

compression, respectively. While these velocities ($\sim 500 \mu/s$) are higher than experimental velocities (0.1 to 10 $\mu m/s$), they are slow enough that stress can be transmitted across the capsid before the separation has changed substantially.

We determine total force from the capsid on each plate and then average the magnitude of these forces to obtain the total compressive force that would be measured by an AFM. The inset in Figure 2 shows that deviations between the forces on the two plates are similar to temporal fluctuations in each. Larger deviations with longer duration are observed if the velocity is too high for stress equilibration. In this and subsequent figures, the mean force is plotted as a function of the plate-to-plate separation, s . While the plate potential has a finite range, it changes so rapidly that the effective space available to the capsid is only slightly smaller than s .

Since capsids are not spherical, their elastic properties should depend on their orientation relative to the compressive axis. We consider two orientations here. Most results are for the case where one of the symmetrically equivalent 2-fold axes is perpendicular to the plates. This corresponds to the z -axis as defined in the structure file [25]. The second situation has a 3-fold axis normal to the plates. This corresponds to the [1,1,1] direction in the structure file and is denoted by [1,1,1]. Note that these orientations represent the initial configuration and the capsids can rotate under the applied load. The observed rotations are relatively small and are discussed further below.

RESULTS

Force-Separation Curves

Figure 2 shows an example of a nanoindentation trajectory for the CCMV capsid. No force is observed for separations greater than 284 Å. The force then rises linearly as s decreases to about 175 Å. This corresponds to a compression by about 35% from the point of first contact, a surprisingly large range of Hookean response, but comparable to what is observed in experiments on capsids. Note that experimental data are typically plotted vs. the displacement of the tip towards the substrate, which becomes more positive as s decreases. One must also be careful to remove the compliance of the AFM cantilever in comparing to experimental numbers.

At the end of the Hookean regime the force drops rapidly by about 40%. A comparable drop is observed in experiments [5, 6]. At still smaller separations the force rises rapidly. Given the observed width of the radial distributions in Figure 1, it is not surprising to find that the top and bottom of the virus are in direct contact at these small separations, leading to strong repulsive forces.

In the regime where the force rises linearly, the nanoindentation process is nearly reversible: An inversion of the direction of motion of the plates results in a force which returns along the same straight line. Once the capsid has been compressed to or beyond the sudden drop in force, the deformation is irreversible. To illustrate this behavior we reversed the velocity of the walls after compressing to 50, 100, 125, 150, 175 and 200 Å and the results are plotted as dotted lines in Fig. 2. The behavior is only reversible for $s=200$ Å. The small drop at s just greater than 175 Å is already signalling the onset of plastic deformation that leads to extremely irreversible behavior. The nature of this plastic deformation is discussed further below.

Figure 3 shows that nanoindentation of a capsid with the [1,1,1] orientation produces very similar results. The diameter along this orientation is slightly bigger, so the force starts at a larger s , but values of F_m and k are very similar to those in Figure 2. The onset of irreversibility also coincides with the end of the Hookean regime. Note that while the capsid was free to rotate, the capsid remained in roughly its initial orientation in both Figures 2 and 3.

The velocity dependence of our results is illustrated in Figure 4. Three different realizations of the system are shown for the velocity considered above, as well as for velocities that are slower and faster by a factor of two. The different realizations at a given speed exhibit essentially the same behavior at large and small separations, but the onset of irreversibility occurs at different forces and separations. This variability suggests that the force drop represents an activated transition from the stable linear regime to another state. The rate dependence is also consistent with this conclusion. In particular, thermal fluctuations have more time to activate the transition as the velocity decreases, and thus the average force at the transition decreases with decreasing velocity. The nature of the transition is discussed further below.

The stiffness of the capsid in the linear regime is relatively insensitive to velocity, with fluctuations comparable to variations with speed. The results are consistent with a very

small (5%) increase in stiffness with speed. A weak linear dependence is expected since atoms are able to relax more closely to the free energy minimum as the velocity decreases. A stronger velocity dependence is observed at very small s . This is the regime where the top and bottom of the capsid are in hard sphere contact. The rapid rise of the repulsive force with decreasing separation makes the system more sensitive to unrelaxed positions in this regime.

The CPMV capsid is found to behave in a qualitatively similar way. As shown in Figure 5, there is a regime where the force rises linearly, followed by a sudden drop in force. The force-separation curve is reversible in the early stages of compression, but becomes irreversible after the end of the linear regime. The main differences between the capsids are that CPMV is much stiffer in the linear regime and fails at a higher yield stress and smaller degree of compression. The peak force $F_m \sim 15 \text{ } \epsilon/\text{\AA}$ is a factor of three larger than for CCMV, while the effective spring constant, $k \sim 0.5 \text{ } \epsilon/\text{\AA}^2$, is an order of magnitude higher. Changing the orientation of the capsid to [111] produces similar results (Figure 6). The peak force is slightly larger, but the difference is within the range of fluctuations between different runs.

The large difference in stiffness of the two viruses is surprising. Continuum theory predicts that $k = 2.25Eh^2/R$ where E is the elastic modulus, h the shell thickness and R the radius [5]. As shown in Fig. 1, CCMV and CPMV have similar radii $R \sim 120 \text{ } \text{\AA}$ and thicknesses $h \sim 20 \text{ } \text{\AA}$. They also have the same interaction energies within our model, and similar numbers of amino acids. Yet the measured stiffnesses would imply elastic moduli that differ by an order of magnitude: $0.007 \text{ } \epsilon\text{\AA}^{-3}$ and $0.07 \text{ } \epsilon\text{\AA}^{-3}$ for CCMV and CPMV, respectively. To put these values in perspective, they are one to two orders of magnitude smaller than the elastic modulus of a Lennard-Jones crystal with the same interactions $E=55 \text{ } \epsilon/\sigma^3 = 1.2 \text{ } \epsilon/\text{\AA}^3$. This large reduction must reflect the fact that the number of bonds constraining the motion of each segment of the protein is relatively small.

Atoms in an fcc crystal have $z = 12$ nearest neighbors or 6 bonds per atom. CCMV and CPMV have only 2 or 3 native contacts per atom, respectively. Including the neighbors along the backbone of the protein, this corresponds to about 6 neighbors for CCMV and 8 for CPMV. The minimum number of neighbors required for stability in 3 dimensions is $z = 4$, and studies of rigidity percolation indicate that the elastic modulus is a strong function z . It seems likely that this explains why increasing the number of native contacts per atom by only 45% (and total bonds per atom by 30%) can increase the effective stiffness of CPMV

by an order of magnitude. The observation that small changes in protein binding can have a dramatic effect on stiffness suggests that further experimental studies may reveal large variations between capsids. We are not aware of any nanoindentation studies of CPMV, but it would be interesting to see if the trends observed in our model are reproduced in experiment.

Changes in bonding

The onset of irreversibility in both CCMV and CPMV is associated with rupture of native contacts rather than a buckling transition like that observed in elastic shell models [5, 11, 12]. Figure 8 shows the total number, n_c , of unbroken native contacts ($r_{ij} < 1.5\sigma_{ij}$) as a function of s . In the initial stage of compression, the number of unbroken contacts remains essentially constant. Thermal fluctuations cause a very small number (0.1%) of bonds to fluctuate in and out of contact, but the structure remains intact. This behavior extends to the end of the Hookean regime where deformation becomes irreversible. At this point n_c drops sharply and then saturates as the virus is compressed further. About half the contacts break during this transition in both CCMV and CPMV.

As seen in the force plots described in the previous section, the onset of irreversibility depends on thermal fluctuations and tends to occur at larger s for slower compression. The drop in n_c always coincides with the onset of irreversibility and shifts in the same way. The dotted line in Fig. 8 illustrates an earlier onset of bond rupture in CCMV at a lower rate. Note that the values of n_c for the different rates coincide before and after rupture occurs. Only the point at which thermal fluctuations lead to bond breaking changes.

Figure 8 shows the total number of contacts, but it is interesting to examine intra and inter-protein bonds separately. For the case of CCMV there are three times as many intraprotein contacts (not counting bonds along the backbone of the protein) as interprotein contacts: 47166 vs. 15300. When bonds begin to break, the number of broken intraprotein bonds is slightly higher, but the fraction of broken bonds is dramatically different. By $s = 149 \text{ \AA}$ over 95% of the interprotein bonds are broken, while more than half the intraprotein bonds remain. This striking result indicates that rupture of the capsid occurs mainly along the joints between proteins, something that would be difficult to capture with homogeneous continuum models.

Interprotein bonds have the same energy parameters as intraprotein bonds, but equilibrium simulations also provide evidence that the joints where proteins meet are weaker. The mean squared variation in the length of native contacts in equilibrium should be given by the thermal energy divided by an effective spring constant that is influenced by bonds to surrounding atoms. For CCMV, the ratio of the mean squared fluctuation to the equilibrium bond length is more than 80% larger for interchain interactions than for intrachain interactions, implying that the interprotein regions are roughly half as stiff as intraprotein regions. This greater fluctuation indicates that there are fewer reinforcing contacts to limit deformation and prevent rupture along the borders of proteins.

In CCMV, proteins fold into kite shaped pieces and three kites (A, B, and C chains) combine to form triangles that tile the surface [24]. There are no intrachain bonds connecting the kites. In CPMV, three trapezoids combine to form triangles. Two trapezoids on adjacent triangles are formed from a single molecule, providing direct intrachain links [24]. Given the mode of rupture, it seems likely that these intrachain bonds between triangles play an important role in the high stiffness and rupture force of CPMV.

Structural Changes in CCMV

In this section we focus on structural changes in the CCMV capsid during deformation, using the trajectory corresponding to Figure 2 to illustrate the changes. Figures 9, 10, and 11 provide different representations of the conformation of the CCMV capsid at various stages of indentation. Figure 9 shows all C^α atoms with different gray scales for different groups of proteins. Snapshots show the evolution of the capsid shape from equilibrium to one of the first states with a significant number of broken bonds, $s = 164 \text{ \AA}$. The walls first flatten and compact the region near the plates, with the size of the flattened region growing as s decreases. The capsid remains relatively undeformed in the central region between walls.

Figure 10 shows a closeup of the 2000 atoms that are closest to the top plate. In the native state, the top of the virus is relatively rough. In the initial stages of deformation ($s = 264 \text{ \AA}$) a few of the highest atoms are pushed down but only a small fraction of the capsid surface feels the hard repulsive potential from the walls. The force is also very small in this range of s , and the stiffness may be slightly smaller than at lower s (Fig. 2). The

number of atoms pushed up against the hard wall potential grows as s decreases. By $s = 239$ there is a pronounced flattened region and parts of all proteins shown are in contact with the surface.

Large structural changes such as buckling and rotation are difficult to identify in all-atom renderings. As noted above, the capsid is constructed from triangular clusters containing three protein chains. A skeleton representation of the structure can be obtained by following the center of mass of the three chains forming each triangle. As shown in Figure 11, the centers of the triangles lie at the vertices of a truncated icosahedron in the native state. In the (110) orientation, a line connecting two vertices is at the top and bottom of the virus. Note that this representation makes it appear that there is a sharp edge at the top and bottom, which would make the configuration appear unstable against rotations. The all-atom rendering shows that the actual surface is fairly spherical and there is no sharp edge.

There are two pentamers and two hexamers that meet at the edges at the top and bottom of the capsid. As s decreases from 284 \AA to 239 \AA these faces become nearly horizontal, and by $s = 214 \text{ \AA}$ many of the associated vertices have become coplanar. There is also a slight clockwise rotation of the capsid that is discussed below. Further compression to $s = 189 \text{ \AA}$ seems to produce buckling with the top (bottom) edge pushed below (above) its neighbors. These structural results are quite similar to those from finite element calculations with a continuum model based on the mass density of the capsid [12]. This model shows that the curvature at the top and bottom of the capsid begins to change sign for compressions greater than 70 \AA , which corresponds to $s = 214 \text{ \AA}$. There is a pronounced region of inverted curvature at a displacement of 100 \AA , which is close to the case of $s = 184 \text{ \AA}$ in Figure 11. It is also interesting that for this capsid orientation the continuum calculation finds little change in the derivative of force with respect to displacement as buckling occurs, while there is a pronounced change for other orientations. Note that we did not observe softening before bond rupture in either (100) or (111) orientations.

For $s \leq 164 \text{ \AA}$ bond breaking becomes important in our simulations. Fig. 11 shows that the capsid has lost most of its structure by $s = 139 \text{ \AA}$. Atoms from the top and bottom of the capsid make direct contact at these small separations, leading to a large hard core repulsive force on the plates. Bond breaking is not included in the continuum calculations and one consequence is that they predict a gradual decrease in the slope of force-displacement curves

as s decreases to 164 Å, while our calculations show a precipitous drop in force at this point.

Figure 12 illustrates the spatial distribution of broken bonds for the simulation shown in Figure 11. Each native contact is characterized by its initial "height" h , or more precisely, the z -coordinate of its geometrical center in the native conformation. The top panel shows the height distribution of native contacts. The bottom panel shows the number with each initial height that are broken at various plate separations. Bond breaking initiates just before s decreases to 164 Å, which is just at the end of the linear portion of the force-displacement curve in Figure 2. Breaking initiates near the bottom of the virus for this trajectory, but failure initiates at the top in other trajectories. As seen in Fig. 11 and continuum calculations, stresses and strains are largest in these extremal regions.

At $s = 164$ Å about 2000 contacts are broken. Decreasing s by just 5 Å ruptures nearly all of the bonds that eventually fail in the bottom region and initiates failure at the top of the capsid. A further decrease by 5 Å has spread the failure over most of the capsid. The number of broken bonds then saturates at lower s as shown in Figure 8. The saturated distribution is illustrated by the results for $s = 139$ Å in Figure 12. Note that the distribution mirrors the number of native contacts, indicating that a fairly constant fraction of the initial bonds has broken throughout all regions of the capsid. As noted above, almost all the bonds binding different proteins together have failed, leading to complete loss of the capsid structure.

We now focus on quantifying the distribution of deformation within the capsid, by considering the z -displacements of individual atoms. They can be illustrated directly through a scatter plot in which the atoms' z -coordinates at separation s , $h(s)$, are plotted against their native z -position, h . Figure 13 shows such scatter plots for the C $^\alpha$ atoms belonging to selected pentamers (3 out of 12) and hexamers (3 out of 20). In each case the n-mers are chosen to represent the top, center and bottom and to prevent overlap of points in the scatter plot. Results are shown for $s = 202$ Å and $s = 164$ Å where bond breaking becomes evident.

At both plate separations the central n-mers are nearly undeformed. The final height differs from the initial height (solid line) in two ways. One is a shift up or down that reflects the small clockwise rotation mentioned in regard to Figure 11. The second is a small change in slope. For both plate separations the slope is 0.93 for the pentamer, while for the hexamer the slope decreases from 0.96 to 0.93 with decreasing s . The decrease in slope from unity results mainly from compression, but is also affected by rotation of the n-mers. The mean

rotation of the capsid is only about 4° for $s = 202 \text{ \AA}$.

The behavior of the outer n-mers is very different. In each case, the largest values of $|h|$ are very close to the height of the walls, $s/2$. As these outer atoms are pushed inwards, they displace the entire thickness of the capsid with them. This leads to a broadening of the scatter plots by an amount comparable to the capsid thickness. Note that the envelope corresponding to the largest values of $|h|$ and the outer edge of the capsid does not merge smoothly with the lines for the central n-mers. This reflects a rapid change in the surface normal at the edge of the central n-mers that is also evident in Figure 11.

To see if the deformations of the capsid in our simulations are consistent with continuum models, we compared them to the finite-element results of Gibbons and Klug [12]. Since the finite element nodes do not correspond to individual atoms, horizontal slices of width 1 \AA at selected heights were chosen and nodes at the inner and outer edges of the capsid were followed. For the finite-element model these are the inner and outer nodes of the mesh and for the molecular model they are the inner and outer C^α atoms. The continuum calculations moved just one wall so that the center of mass moved. We have corrected for this so that zero height corresponds to the center of mass in both cases.

Figures 14 and 15 compare the finite-element and molecular models for two plate separations. Figure 14 shows molecular model results for $s = 202 \text{ \AA}$ which corresponds to a compression of $Z = 82 \text{ \AA}$. These results are compared to finite element results at $Z = 75 \text{ \AA}$. Figure 15 presents results for $Z = 116 \text{ \AA}$ in the continuum model and $Z = 120 \text{ \AA}$ in the molecular model, which corresponds to the onset of bond breaking ($s = 164 \text{ \AA}$).

For both separations the molecular results show a spread in final heights for atoms with the same small initial height [36]. This reflects the symmetry breaking rotation of the capsid that is evident in Figures 11 and 13. Symmetry breaking is suppressed in the continuum model by the lack of thermal fluctuations and the fact that a friction force was imposed to suppress sliding of the virus relative to the wall. As shown in Fig. 13, the spread in results for the molecular model results from coherent shifts in the height of each n-mer through a relatively rigid rotation. For each n-mer there is a linear relation between initial and final height. The continuum model shows a linear relation for all nodes with slightly different slopes for the inner and outer atoms. A least mean squares fit to heights of all nodes between $\pm 40 \text{ \AA}$ gives 0.90 for the continuum model at $Z = 75 \text{ \AA}$. The same fit for atoms in the molecular model gives a slope of 0.94, indicating that there is significantly less

strain in the central region.

The deviations between continuum and molecular models are slightly larger near the top and bottom of the capsid. Both show a spread between inner and outer edges, because the outer surface is in contact with the wall and the inner surface remains at a fixed distance below the outer surface. The continuum model gives a smoother curve for the outer surface, while the outer height appears to vary non-monotonically in the molecular model. A local dip in final height at an initial height of around 100 Å is visible for both wall separations. The region where the final height corresponds to contact with the wall also extends over a larger range of heights in the molecular model. This is consistent with less strain being accommodated in the central region, and more in the regions near the walls.

The radial strain for both models was also calculated. Defining \vec{r} as the initial position relative to the center of mass and \vec{dr} as the change in this vector, the radial strain $\epsilon_r = \vec{r} \cdot \vec{dr} / \vec{r} \cdot \vec{r}$. Figure 16 contrasts the molecular and continuum response for $s = 202$ Å and $Z = 75$ Å, respectively. In both cases, the strain is negative at large $|z|$ where compression has flattened the top and bottom. In the central region the capsid bows out and ϵ_r is positive. For the continuum case the inner and outer regions form smooth parabolas that cross at intermediate z . There is some symmetry breaking due to the onset of buckling on one side. In the central region, the radius expands by an average of about 15%. The molecular model shows substantially less expansion, with an average of less than 5%. The envelope of the data is also less smooth, showing a nearly constant expansion in the center and a rapid change in slope for $|z| > 60$ Å. This is consistent with the apparent change in slope in Figure 13 and may reflect localized bending at joints between proteins in this region. Note that Fig. 15 shows that the flattened region of the capsid has extended down to atoms with initial heights of order 60 Å by $s = 164$ Å. It may be that this leads to failure because strain can no longer be accommodated by the outer regions.

To illustrate the development of deformations with decreasing separation, the center of mass height \bar{z} and rms variation Δz was calculated for atoms comprising each of the n-mers. Figures 17 and 18 show results for all pentamers and hexamers, respectively. The locations of the centers of mass indicate a fairly smooth transition to a flattened "sandwich" state as the wall separation becomes comparable to the thickness of capsid walls. At large s , the height of the top and bottom n-mers changes much more rapidly than those in the center, indicating yet again that strain is concentrated in the regions near the walls. The

mean displacement of n-mers at the same intermediate height shows a relatively smooth splitting, that is associated with the symmetry breaking rotation seen before. The splitting is not sudden and is reversible when the load is removed. The mean rotation is about 4° for $s = 202 \text{ \AA}$.

Note that one of the n-mers in each pair stays at a nearly constant height while the other n-mer moves linearly towards the center. In contrast, the n-mers that start in the center move away from the center with symmetry related pairs displacing by equal and opposite amounts. Once significant bond-breaking sets in, the heights change rapidly. Note that the relative height of outer and more central n-mers changes sign, indicating buckling. It is also interesting that the centers of the outer n-mers become equal to the centers of more central n-mers at the point where bond breaking sets in. These heights are also equal to the height where rapid bending is evident in Fig. 16.

The trends in the rms height change mirror the shifts in the mean. Initially there is a fairly linear increase in Δz with the greatest slope for the n-mers farthest from the equator. The rms displacements are very large, comparable to the mean motion in many cases. This reflects the rotation of the outer n-mers as they move into contact with the wall. When bonds begin to break, all of the n-mers show rms variations of 20 to 40 \AA which is comparable to the thickness of the capsids and to the plate separation at the smallest s . The n-mers are made up of several proteins that are no longer bonded together at small s and thus deform incoherently.

SUMMARY AND CONCLUSIONS

A coarse-grained molecular model was used to study the mechanical response of CCMV and CPMV. Both show a linear elastic response at small deformations followed by a rapid drop in force. The response is reversible in the elastic regime and becomes irreversible after the force drop due to rupture of bonds within the capsid. Although the two capsids have similar radii, widths and densities, their mechanical response is dramatically different. CPMV is an order of magnitude stiffer and fails at a much smaller compression and much larger peak force.

The dramatic differences between CCMV and CPMV are the result of a relatively modest change in the number of bonds. Insight to this dependence comes from comparing the

response to elastic shell models. While the effective modulus from fits to CPMV is an order of magnitude larger than that for CCMV, it is more than an order of magnitude smaller than that of an fcc crystal with the same bonding energies. The crystal would also fail at much smaller deformations. The mean number of neighbors drops from 12 in the fcc crystal to 8 in CPMV and only 6 in CCMV. Four are required to provide mechanical stability in 3 dimensions and studies of rigidity percolation show that the modulus is a strong function of the number and distribution of neighbor bonds. Thus viruses may be able to alter their stiffness and ability to accommodate large strains through small variations in the number of interprotein bonds. It would be interesting to perform experiments on CPMV and other virus capsids to see if the effective modulus does vary by an order of magnitude and whether this mechanical property is correlated to the environment or biological functions of the different capsids.

Elastic continuum models produce a nonlinear drop in force when the shell buckles. Since there are no thermal fluctuations, buckling occurs at a well-defined displacement where the system becomes linearly unstable. In the molecular model the force drop is associated with rupture of almost all the interprotein bonds, allowing the capsid to fragment. The capsid did not reform on the time scale of our simulations, but experiments show some recovery over times of order minutes [5].

The simulation results are consistent with the force drop being an activated transition where breaking of a few bonds leads to stress transfer and a cascade of additional bond breaking. In particular, different trajectories at the same deformation rate follow a common force curve before and after the transition, but the transition occurs at different displacements. As the wall separation is decreased more slowly, there is more time for thermal activation and the transition occurs at lower forces and displacements. Experiments show a similar trend in the onset of irreversibility with velocity [5], while there is no shift in the location of the buckling transition in deterministic continuum models. As is typical of activated transitions, the stiffness in the elastic region is relatively insensitive to deformation rate [18]. An unusual activated rate dependence of the stiffness was observed in recent all-atom simulations with a much smaller probe and higher velocities [17]. As pointed out by the authors of this study, the rate dependence they observe suggests that their deformation rates were too high to allow the virus structure to relax completely.

Quantitative comparison to experiments is complicated by rate dependence and uncer-

tainties in the binding energy within our molecular model. The latter also leads to uncertainties in the appropriate temperature. Our slowest rates are two to four orders of magnitude faster than experimental rates and the wall displacement that produces irreversibility ranges from 150 to 90 Å. The range of rates and statistics are too small to extrapolate these results to the displacements of about 40 Å where irreversibility is observed in experiments. Continuum models give buckling at roughly twice this displacement, but buckling does not produce a strong drop in the force, particularly for the (100) orientation. The molecular model gives buckling at about the same displacement as the continuum model and also shows that it does not have a strong impact on the stiffness. The sharp force drop in the molecular model occurs at larger deformations when bonds begin to break. At the rates considered here, bonds break after the buckling transition, and the onset of breaking shifts relatively rapidly with velocity. One might expect that buckling produces highly strained bonds that are more susceptible to activated rupture and that the velocity dependence might become much slower when the transition occurs at the smaller displacements found in experiments.

Experiments on CCMV at pH=5 give a peak force of $F_m = 0.60 \pm 0.04$ nN and a stiffness (-dF/ds) of $k = 0.15 \pm 0.01$ N/m in the elastic region [5]. In our simulations, $k \approx 0.05$ $\epsilon/\text{Å}^2$ and the peak force is about 4 $\epsilon/\text{Å}$ at the lowest velocity. Using a binding energy of $\epsilon = 110$ pNÅ, these values correspond to $k \sim .055$ N/m and $F_m \sim 0.4$ nN, which are of the same order of magnitude as measured values. It is not surprising that agreement is better for F_m since ϵ was obtained from fits of simulated force curves during mechanical unfolding to experiments that, as here, were done at lower rates. Increasing ϵ would increase both F_m and k , but lowering the rate would bring F_m back toward the experimental value and also decrease the displacement at failure toward the 40 Å found in experiment. A larger ϵ would also decrease the effective temperature, which also increases k and F_m . Thus the quantitative agreement is as good as can reasonably be expected from a coarse-grained model.

The local deformations within the CCMV capsid were compared to continuum calculations. While the continuum model captures the gross features of the deformation there are deviations that must reflect variations in the local elastic properties due to the distribution of native contacts. In the molecular model, more of the deformation is accommodated in the top and bottom of the capsid. The central region is compressed less, and also shows substantially less radial expansion than the continuum model. There is a relatively large change in angle at a height of about 60 Å that suggests bending. Given the other evidence

that the regions between proteins are less rigid, it seems likely that bending is localized between proteins. More detailed studies of local deformations and stresses is in progress.

Discussions with R. Bruinsma, W. Klug, and A. Zlotnick are warmly appreciated. We thank W. S. Klug and M. M. Gibbons for providing us with results from their continuum model. This work has been supported by the grant N N202 0852 33 from the Ministry of Science and Higher Education in Poland, the EC FUNMOL project under FP7-NMP-2007-SMALL-1, and by the European Union within European Regional Development Fund, through grant Innovative Economy (POIG.01.01.02-00-008/08). Partial support for this work was also provided by the National Science Foundation under Grant No. DMR-0454947.

-
- [1] A. Evilevitch, L. Lavelle, C. M. Knobler, E. Raspaud, and W. M. Gelbart, Osmotic pressure inhibition of DNA ejection from phage. *Proc. Natl. Acad. Sci. USA* **100**, 9292-9295 (2003).
 - [2] M. Buenemann and P. Lenz, Mechanical limits of viral capsids. *Proc. Natl. Acad. Sci. USA* **104**, 9925-9930 (2007).
 - [3] M. Buenemann and P. Lenz, Elastic properties and mechanical stability of chiral and filled capsids. *Phys. Rev. E* **78**, 051924 (2008).
 - [4] I. L. Ivanovska, P. J. de Pablo, B. Ibarra, G. Sgalari, F. C. MacKintosh, J. L. Carrascosa, C. F. Schmidt, and G. J. L. Wuite, "Bacteriophage capsids: Tough nanoshells with complex elastic properties." *Proc. Natl. Acad. Sci. U.S.A.* 101, 7600 (2004).
 - [5] J. P. Michel, I. L. Ivanovska, M. M. Gibbons, W. S. Klug, C. M. Knobler, G. J. L. Wuite, and C. F. Schmidt, Nanoindentation studies of full and empty viral capsids and the effects of capsid protein mutations on elasticity and strength. *Proc. Natl. Acad. Sci. USA* **103**, 6184-6189 (2006).
 - [6] W. S. Klug, R. F. Bruinsma, J.-P. Michel, C. M. Knobler, I. L. Ivanovska, C. F. Schmidt, and G. J. L. Wuite, Failure of viral shells, *Phys. Rev. Lett.* **97**, 228101 (2006).
 - [7] M. Rief, M. Gautel, F. Oesterhelt, J. M. Fernandez, and H. E. Gaub Reversible unfolding of individual titin immunoglobulin domains by AFM. *Science* **276**, 1109-1112 (1997).
 - [8] M. Carrion-Vasquez, A. F. Oberhauser, S. B. Fowler, P. E. Marszalek, P. E. Broedel et al. Mechanical and chemical unfolding of a single protein: a comparison. *Proc. Natl. Acad. Sci. USA* **96**, 3694-3699 (1999).

- [9] A. Valbuena, J. Oroz, R. Hervás, A. M. Vera, D. Rodríguez, et al. On the remarkable robustness of scaffoldins. *Proc. Natl. Acad. Sci. USA.* (2009).
- [10] G. A. Vliegenthart and G. Gompper, Mechanical deformation of spherical viruses with icosahedral symmetry. *Biophys. J.* **91**, 834-839 (2006).
- [11] M. M. Gibbons and W. S. Klug, Nonlinear finite-element analysis of nanoindentation of viral capsids. *Phys. Rev. E* **75**, 031901 (2007).
- [12] M. M. Gibbons and W. S. Klug, Influence of nonuniform geometry on nanoindentation of viral capsids. *Biophys. J.* **95**, 3640-3649 (2008).
- [13] E. C. Dykeman and O. F. Sankey, Low frequency mechanical models of viral capsids: an atomistic approach. *Phys. Rev. Lett.* **100**, 028101 (2008).
- [14] F. Tama and C. L. Brooks III, The mechanism and pathway of pH induced swelling in cowpea chlorotic mottle virus. *J. Mol. Biol.* **318**, 733-747 (2002).
- [15] M. K. Kim, R. L. Jernigan, and G. S. Chirikjian, An elastic network model of HK97 capsid maturation. *J. Struct. Biol.* **143**, 107-117 (2003).
- [16] F. Tama and C. L. Brooks III, Diversity and identity of mechanical properties of icosahedral viral capsids studied with elastic network normal mode analysis. *J. Mol. Biol.* **345**, 299-314 (2005).
- [17] M. Zink and H. Grubmueller, Mechanical properties of the icosahedral shell of southern bean mosaic virus: a molecular dynamics study. *Biophys. J.* **96** 1350-1363 (2009).
- [18] H. A. Kramers, Brownian motion in a field of force and the diffusion model of chemical reactions. *Physica (Utrecht)* **7**, 284 (1940)
- [19] M. Cieplak and T. X. Hoang, Universality classes in folding times of proteins *Biophysical Journal* **84** 475-488 (2003).
- [20] M. Cieplak, T. X. Hoang and M. O. Robbins, Thermal effects in stretching of Go-like models of titin and secondary structures. *Proteins: Struct. Funct. Bio.* **56**, 285-297 (2004).
- [21] J. I. Sulkowska and M. Cieplak, Mechanical stretching of proteins – a theoretical survey of the Protein Data Bank. *J. Phys.:Cond. Mat.* **19**, 283201 (2007).
- [22] T. Lin, Z. Chen, R. Usha, C. V. Stauffacher, J.-B. Dai, T. Schmidt, and J. E. Johnson, The refined crystal structure of cowpea mosaic virus at 2.8 Å resolution. *Virology* **265**, 20-34 (1999).
- [23] Q. Wang, E. Kaltgrad, T. Lin, J. E. Johnson, and M. G. Finn, Natural supramolecular building

- blocks: wild-type cowpea mosaic virus. *Chem. and Biol.* **9**, 805-811 (2002).
- [24] J. A. Speir, S. Munshi, G. Wang, T. S. Baker, and J. E. Johnson, Structures of the native and swollen forms of cowpea chlorotic mottle virus determined by X-ray crystallography and cryo-electron microscopy. *Structure* **3** 63-78 (1995).
- [25] M. Carrillo-Tripp, C. Shepherd, I. A. Borelli, S. Venkataraman, G. Lander, P. Natarajan, J. E. Johnson, C. L. Brooks III, and V. Reddy, VIPERdb2: an enhanced and web API enabled relational database for structural virology, *Nucl. Acids Res.* **37** D436-D442 (2009); <http://vipperdb.scripps.edu/>.
- [26] J. Tsai, R. Taylor, C. Chothia, and M. Gerstein, The packing density in proteins: Standard radii and volumes. *J. Mol. Biol.* **290**, 253-266 (1999).
- [27] J. I. Sułkowska and M. Cieplak, Selection of optimal variants of Go-like models of proteins through studies of stretching, *Biophys. J.* **95**, 3174-3191 (2008)
- [28] M. Sikora, J. I. Sułkowska, and M. Cieplak, Mechanical strength of 17 132 model proteins and cysteine slipknots. *PLoS Comp. Biology*, (in press).
- [29] M. Cieplak and P. E. Marszalek, Mechanical unfolding of ubiquitin molecules, *J. Chem. Phys.* **123** 194903 (2005)
- [30] M. P. Allen and D. J. Tildesley, "Computer simulations of liquids". Oxford University Press, New York, 1987.
- [31] Grest, G.S., Kremer, K. Molecular dynamics simulation for polymers in the presence of a heat bath. *Phys. Rev. A* **33** 3628-31, 1986.
- [32] T. Veitshans, D. Klimov, and D. Thirumalai, Protein folding kinetics: time scales, pathways, and energy landscapes in terms of sequence-dependent properties. *Folding Des.* **2**, 1-22 (1997).
- [33] P. Szymczak and M. Cieplak, Stretching of proteins in a uniform flow, *J. Chem. Phys.* **125**, 164903 (2006).
- [34] W. A. Steele, Physical interaction of gases with crystalline solids. 1. Gas-solid energies and properties of isolated adsorbed atoms. *Surf. Sci.* **36**, 317-352 (1973)
- [35] M. Cieplak, E. D. Smith, and M. O. Robbins, Molecular origins of friction: the force on adsorbed layers. *Science* **265**, 1209-1212 (1994).
- [36] It should be noted that the widths of the scatter plots in the equatorial regions shown in Figure 13 are smaller than those shown in the top panels of Figures 14 and 15. This is simply because only single equatorial hexamers and pentamers are displayed in the previous figure

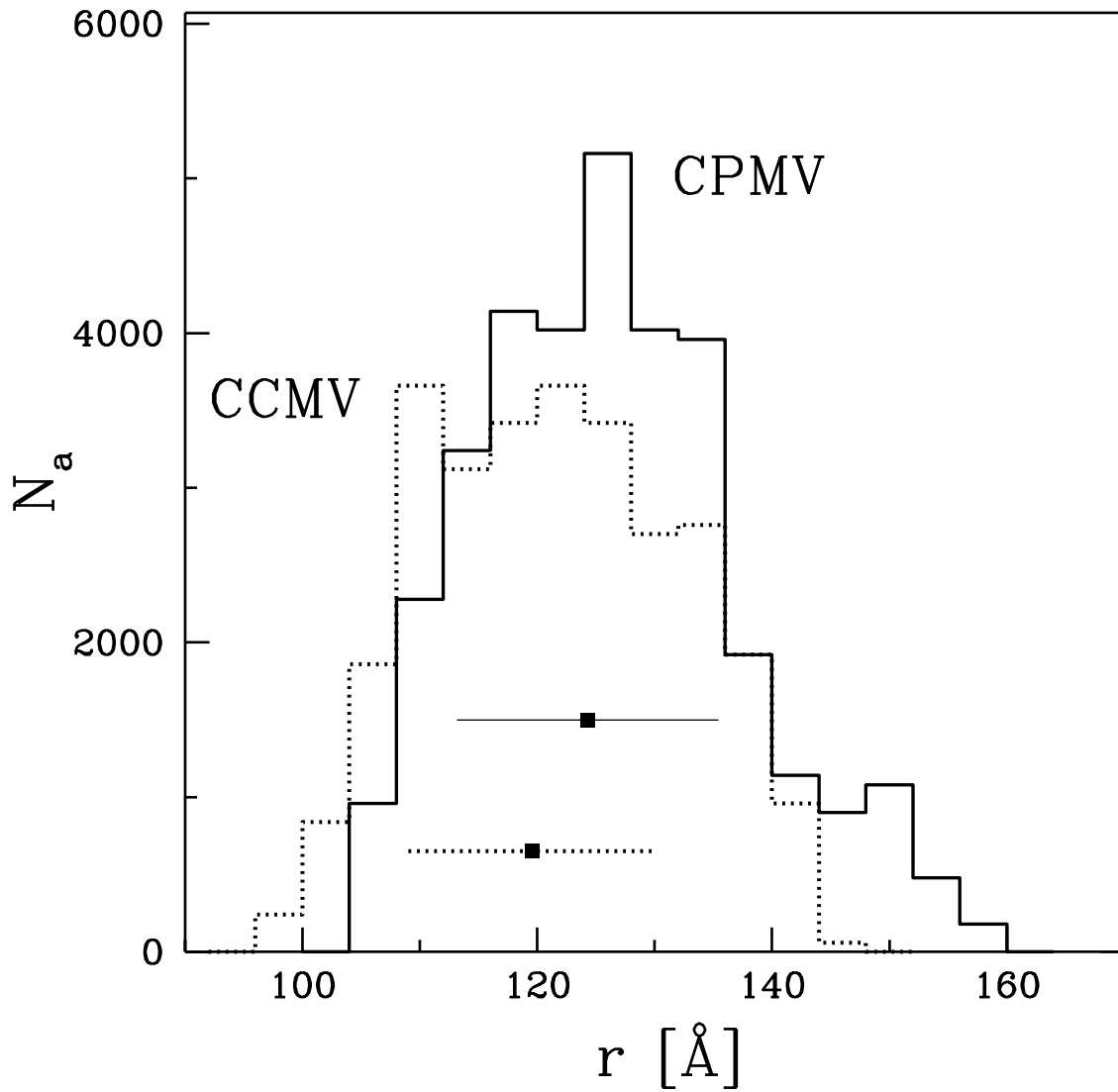


FIG. 1: The radial distributions of the C^α atoms in the CCMV (dotted line) and CPMV (solid line) capsids. The solid squares indicate the mean radii and the horizontal lines show the sizes of the standard deviations.

and all n-mers are considered now.

FIGURE CAPTIONS

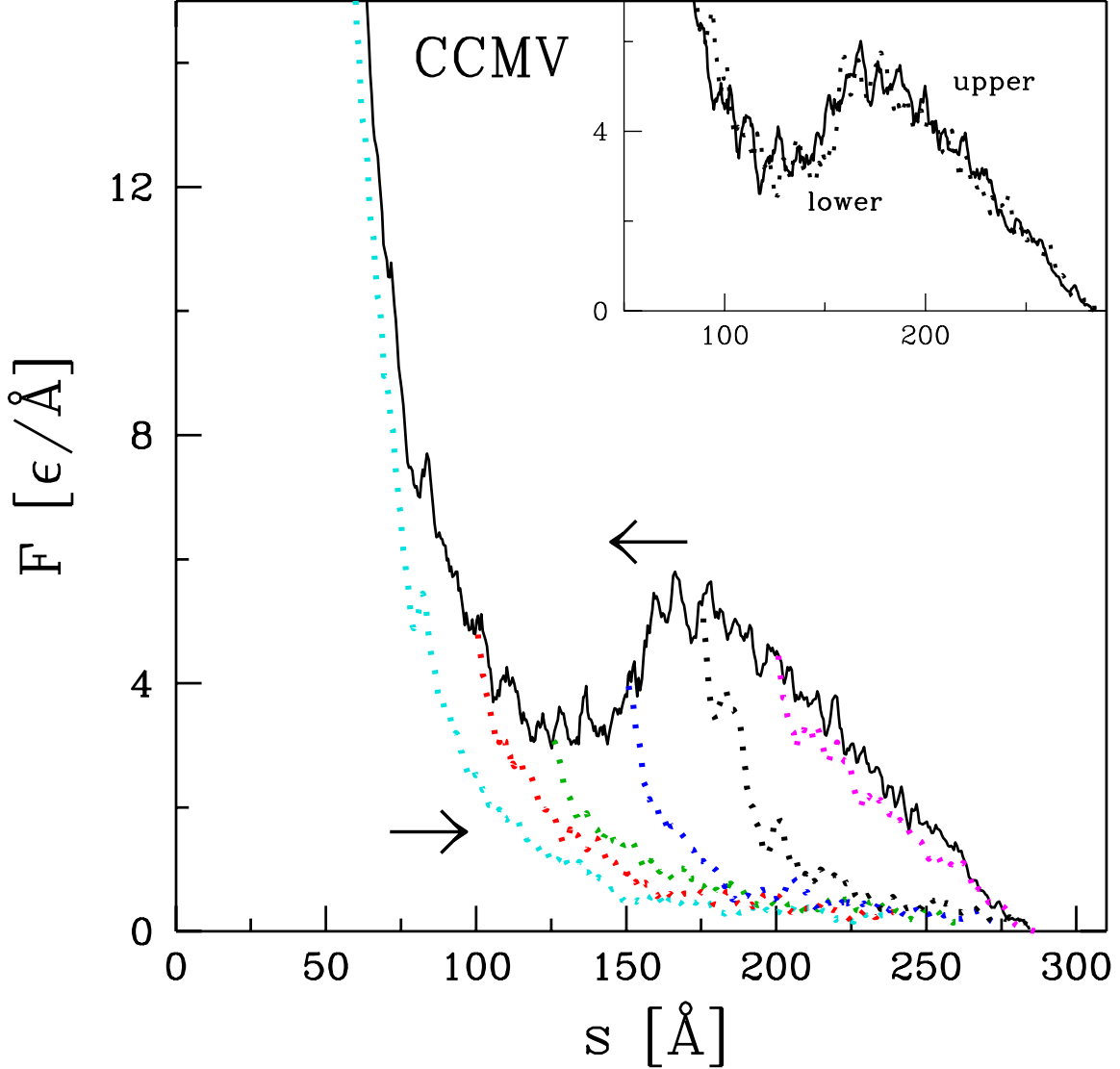


FIG. 2: Force on confining plates from CCMV capsid atoms as a function of the plate-plate separation in one trajectory corresponding to $v_p=0.0025 \text{ \AA}/\tau$. The solid line corresponds to nanoindentation. The dotted lines show the force observed when the plates move back at the same speed after reaching the separation indicated by detachment of dotted lines from the solid line. The inset shows the separate forces acting on the top (solid) and bottom (dashed) plates. The average of these forces is the solid line in the main figure.

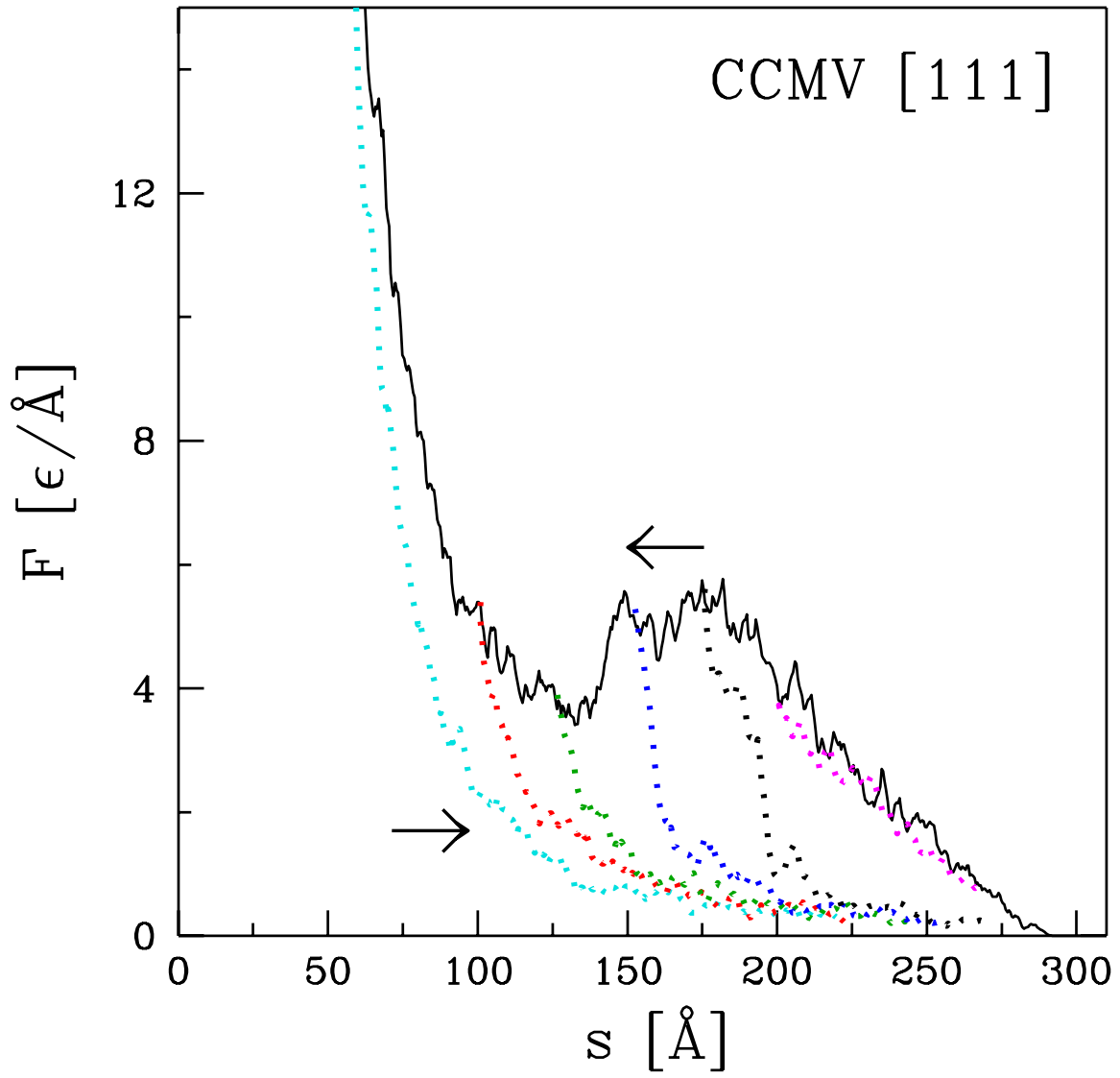


FIG. 3: Similar to Figure 2 but for nanoindentation along the [1,1,1] direction.

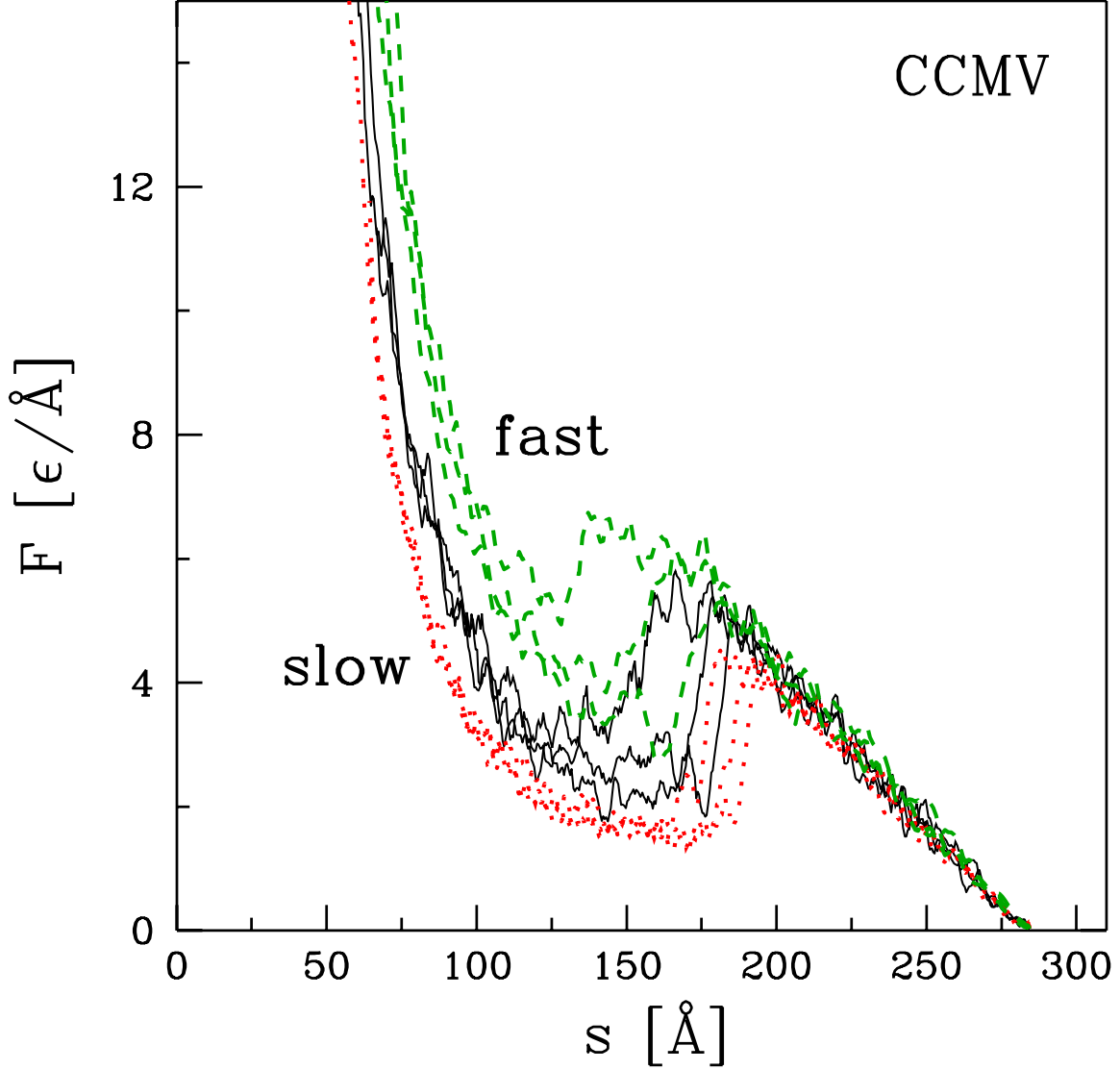


FIG. 4: Variation of the force on a CCMV capsid with separation for different trajectories and compression speeds. The solid lines in the center correspond to three trajectories at $v_p = 0.0025 \text{ \AA}/\tau$. The three dotted and dashed lines correspond to trajectories at half and twice this speed, respectively.

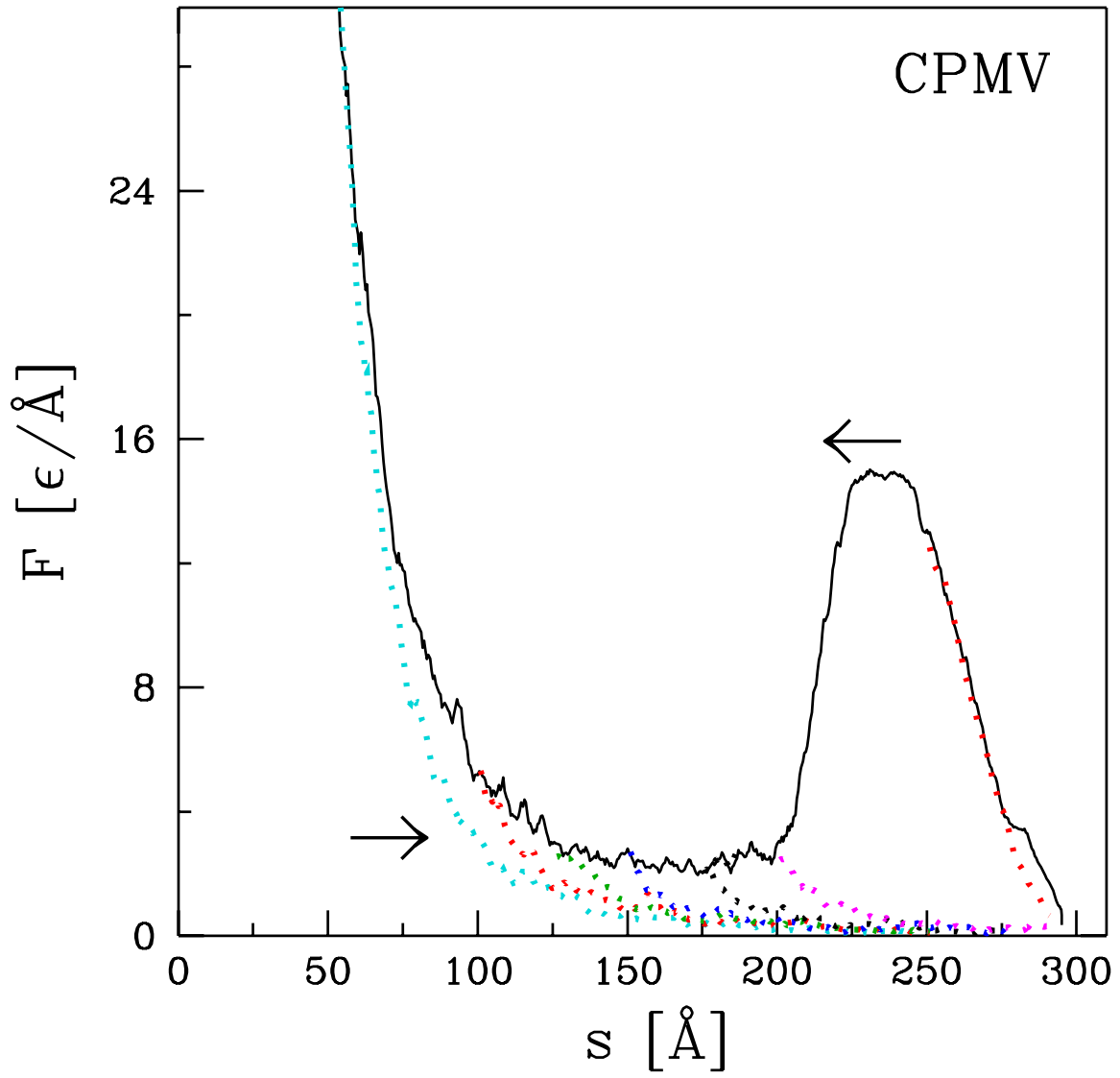


FIG. 5: Similar to Figure 2 but for CPMV.

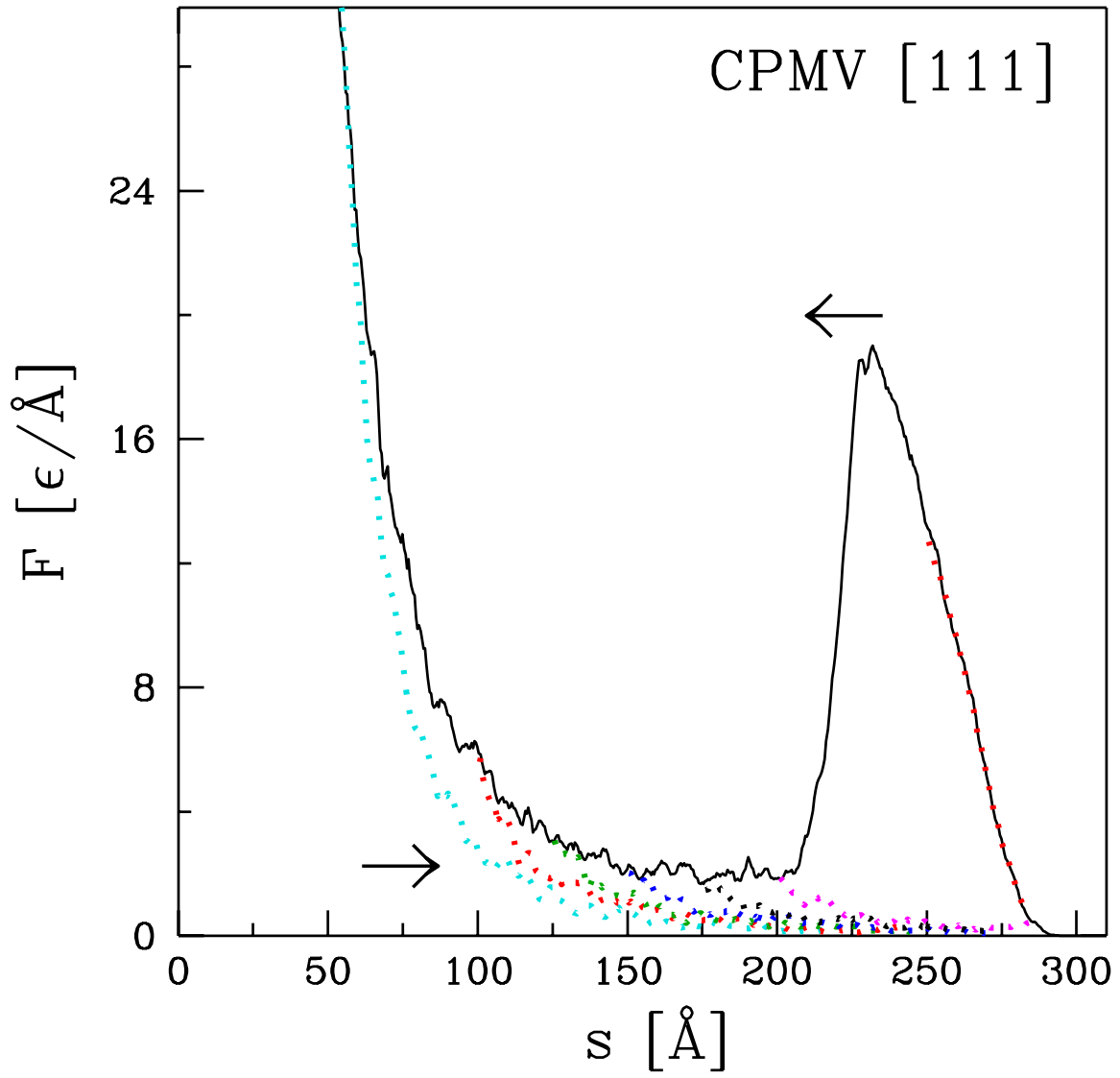


FIG. 6: Similar to Figure 5 but for nanoindentation along the [1,1,1] direction.

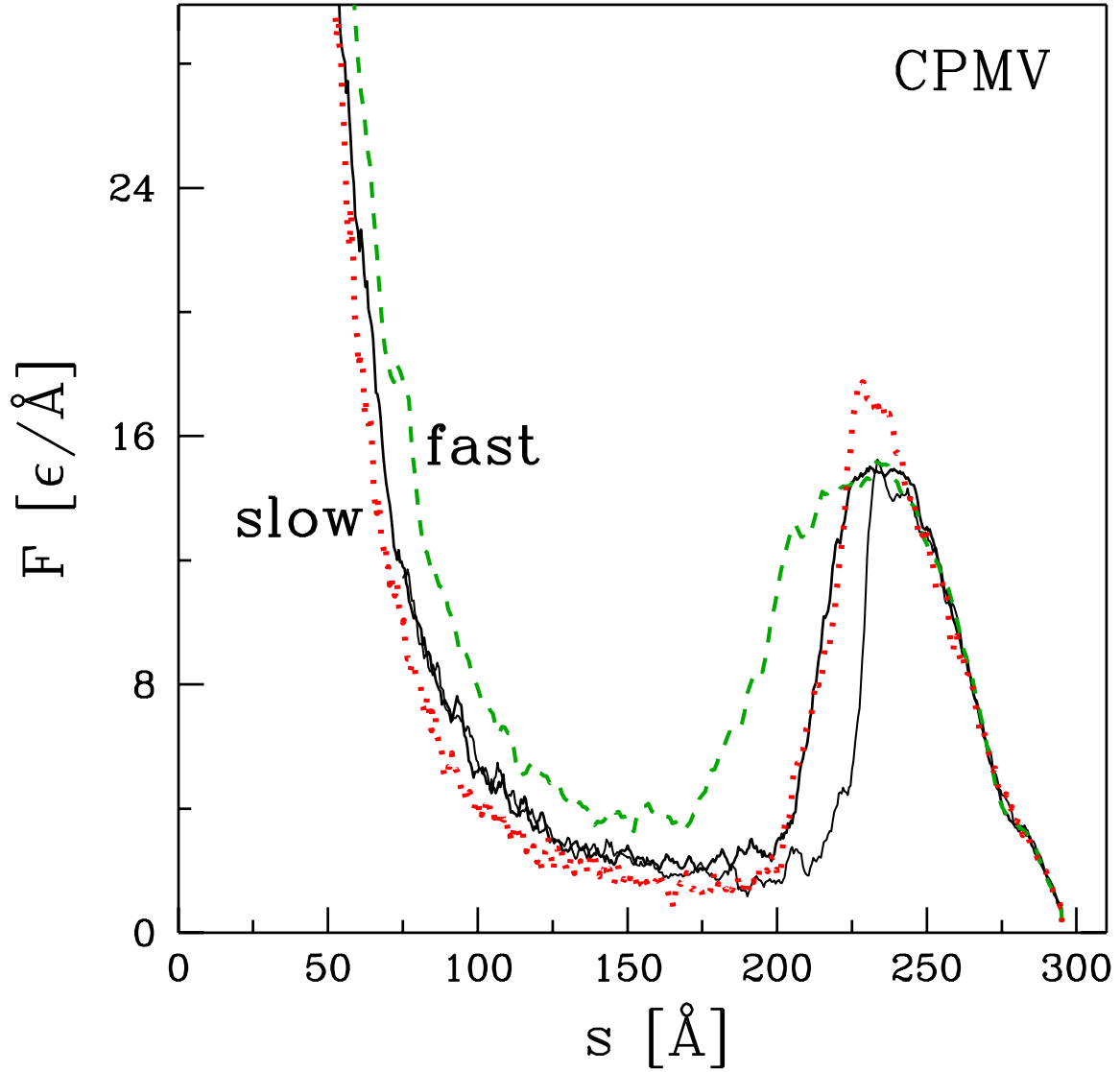


FIG. 7: Similar to Figure 4 but for the model CPMV. Two trajectories are shown for $v_p = 0.0025$ $\text{\AA}/\tau$ (solid lines) and single trajectories at half (dotted line) and twice (dashed line) this speed.

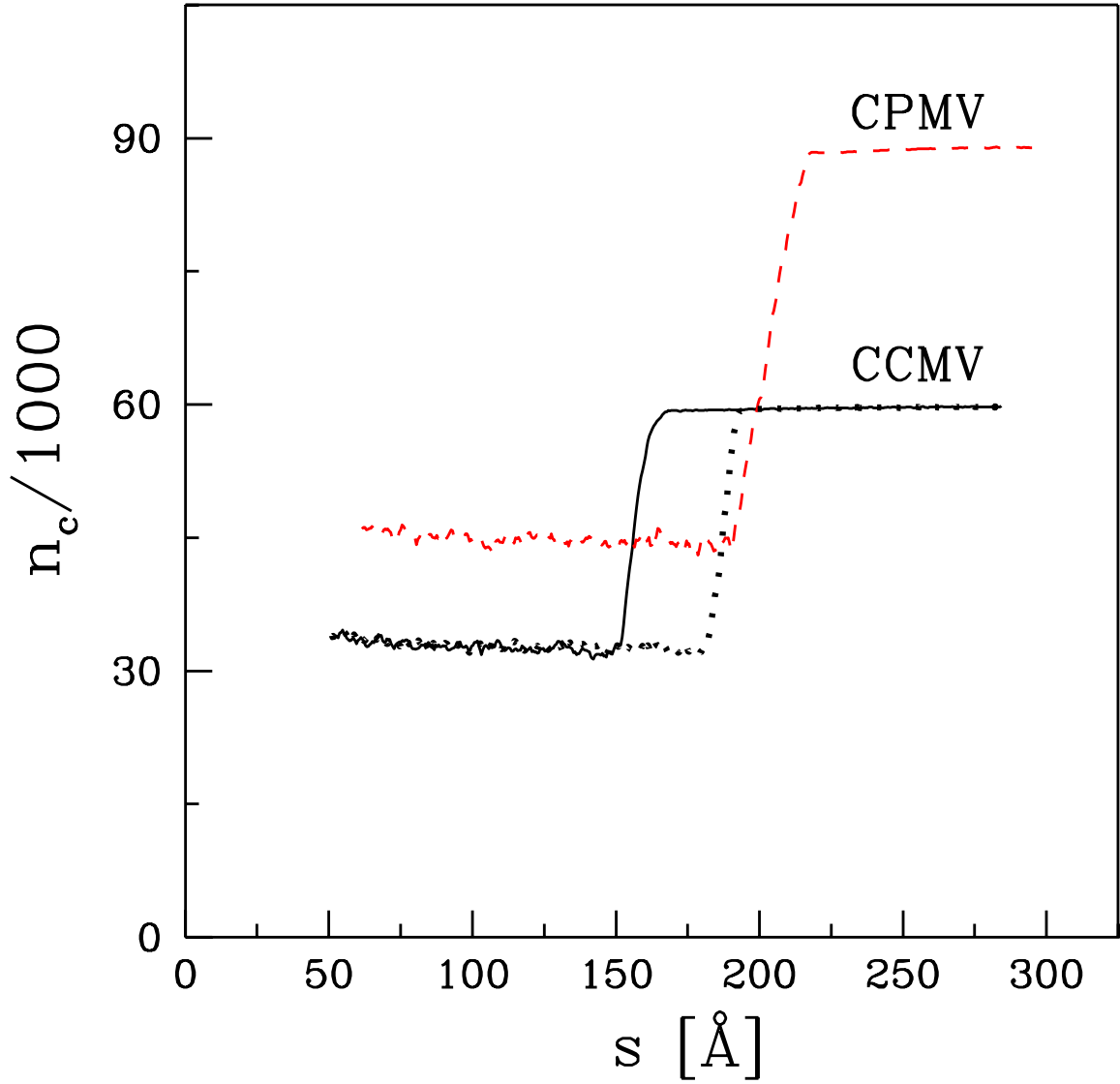


FIG. 8: The number of native contacts that remain unruptured as a function of s for CCMV (solid line) and CPMV (dashed line) in trajectories corresponding to those shown in Figures 2 and 5, respectively. A native contact is considered unruptured if the two amino acids are within a distance of $1.5 \sigma_{ij}$. The dotted line is for compression of CCMV at half the speed and corresponds to the lowest trajectory in Figure 4.

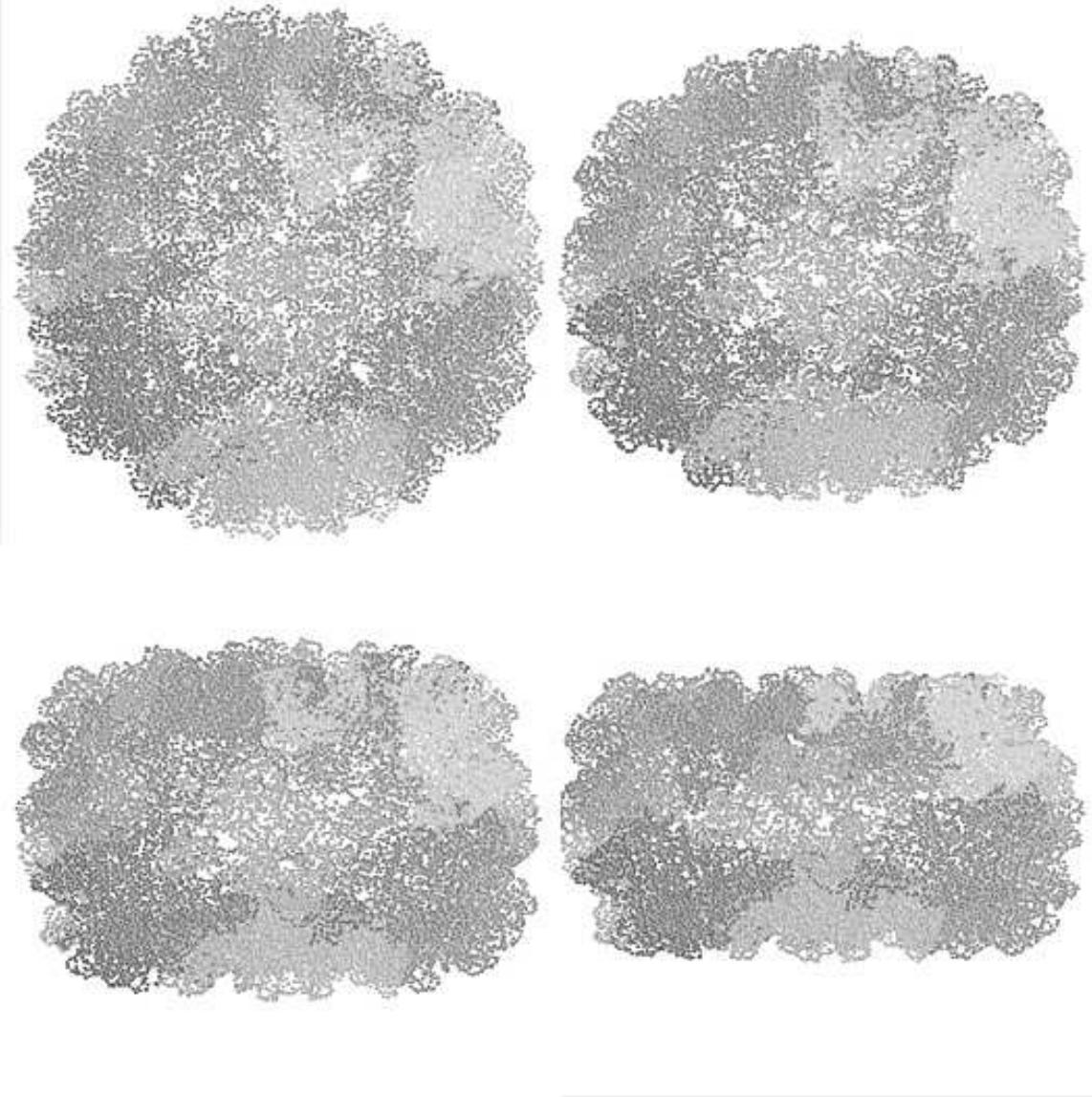


FIG. 9: The structure of the CCMV capsid with all C^α locations shown at $s=284$ Å (top left), 239 Å (top right), 189 Å (bottom left, and 164 Å (bottom right). The smallest value of s corresponds to the start of the nonlinear regime.

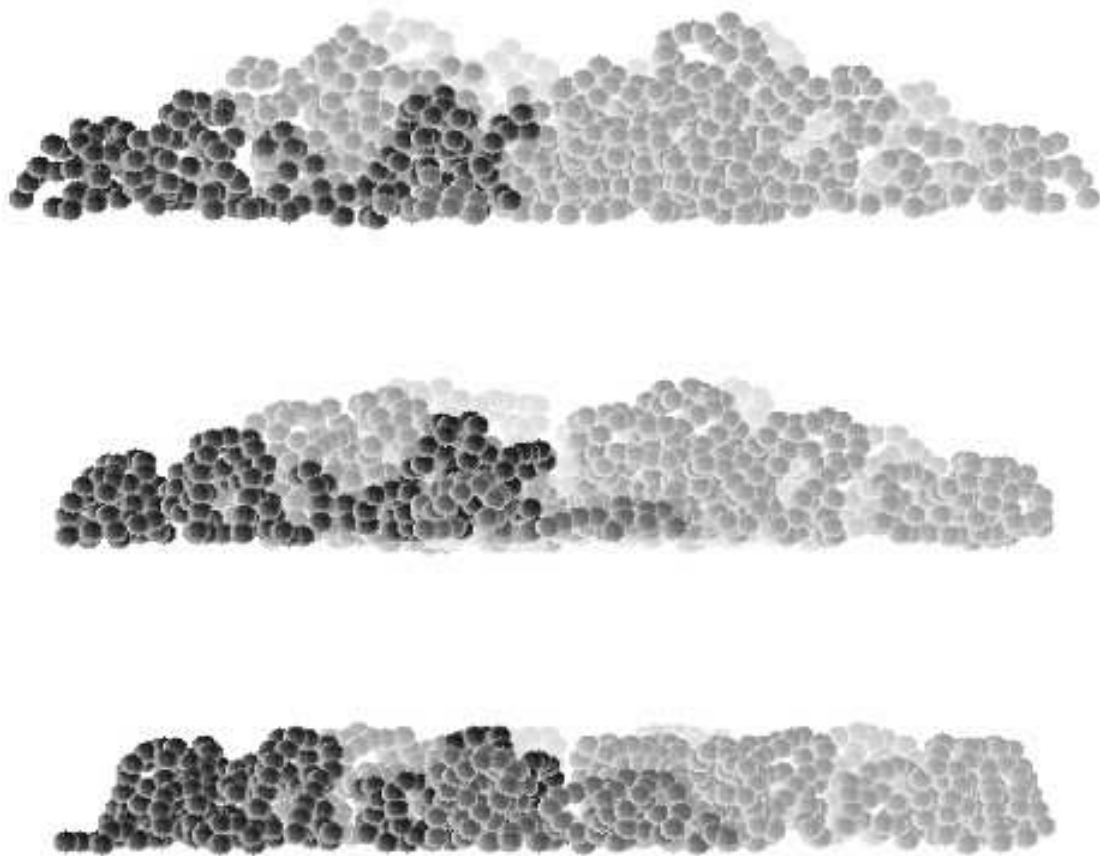
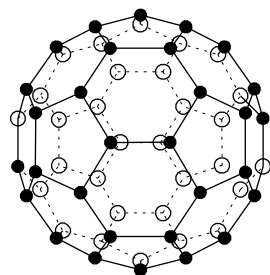
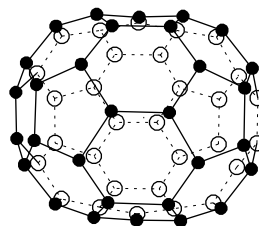


FIG. 10: Snapshots of the 2000 highest C^α atoms for s equal to 284 Å, 264 Å, and 239 Å, from top to bottom. All of these snapshots are in the Hookean regime.

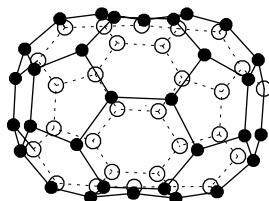
CCMV



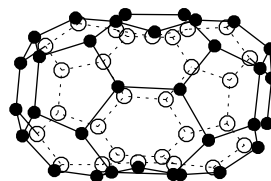
$s=284 \text{ \AA}$



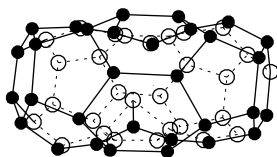
$s=239 \text{ \AA}$



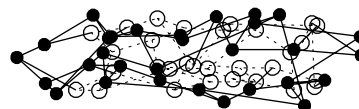
$s=214 \text{ \AA}$



$s=189 \text{ \AA}$



$s=164 \text{ \AA}$



$s=139 \text{ \AA}$

FIG. 11: The vertex representation of the CCMV capsid at various stages of indentation characterized by the indicated values of s . The solid circles are closer to the viewer and the open circles are in back.

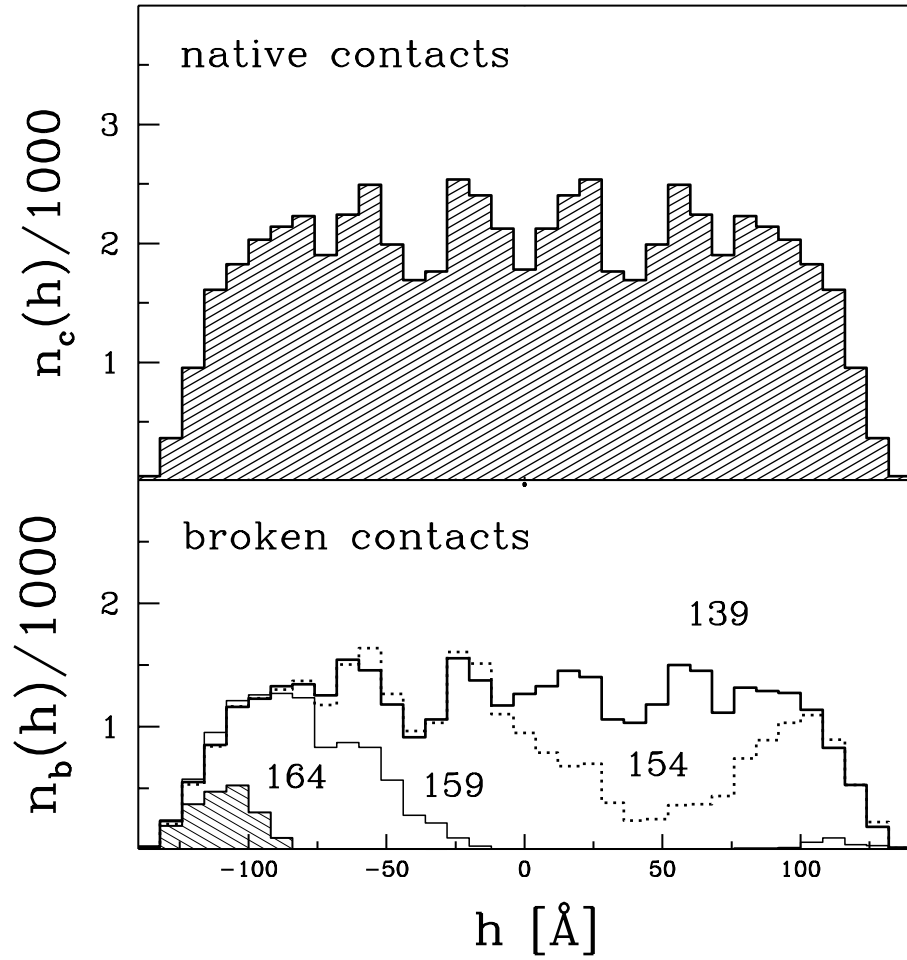


FIG. 12: The top panel shows the z -dependent distribution of the native contacts, $n_c(h)$, as explained in the text. The bottom panel shows the distributions of contacts that are broken at the indicated values of s in Å.

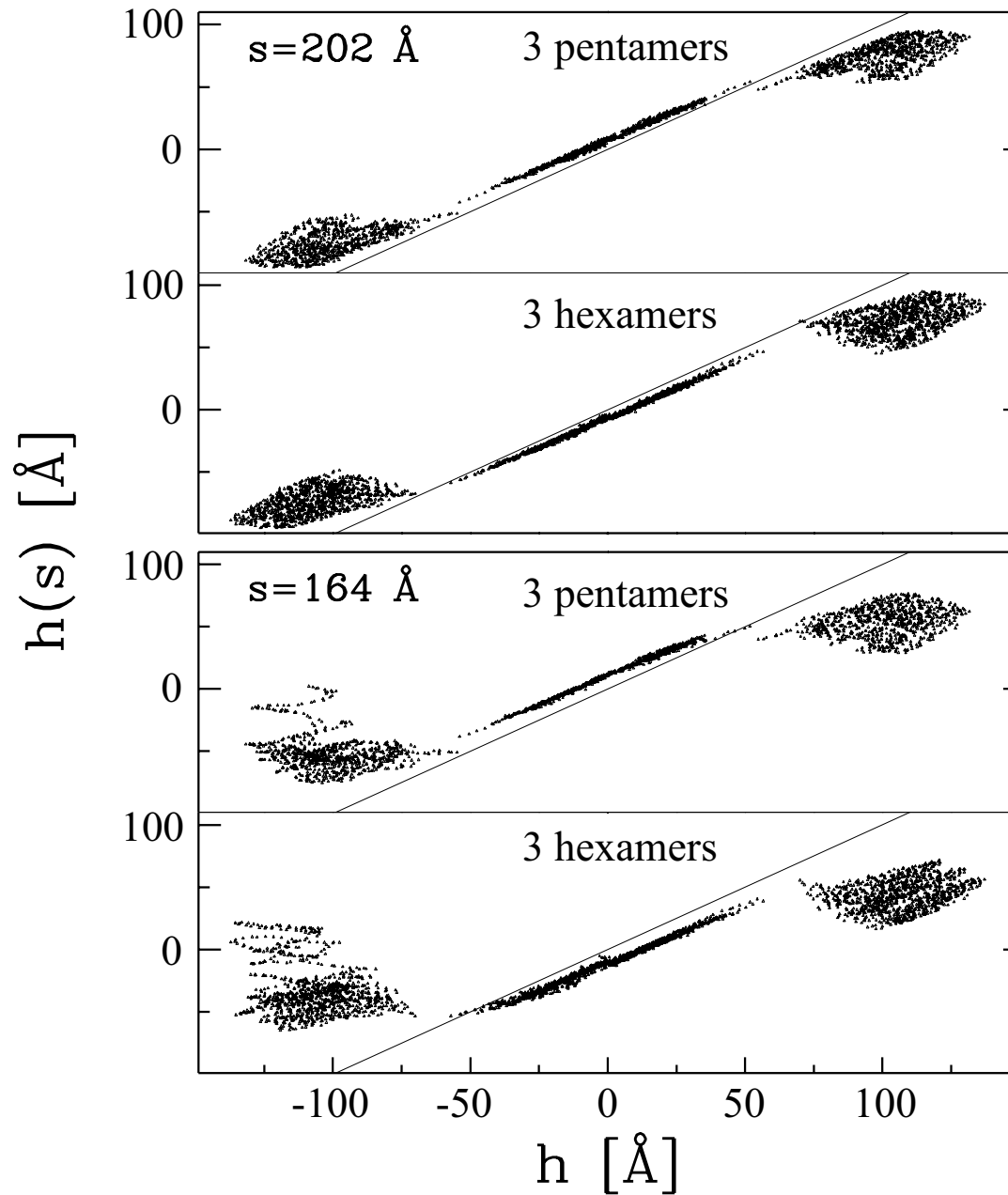


FIG. 13: Scatter plots of final heights of C^α atoms as a function of initial heights in the native structure. The top two panels are for $s=202 \text{ Å}$ and the bottom two panels are for $s=164 \text{ Å}$. Hexamers and pentamers were selected to represent the polar and equatorial regions.

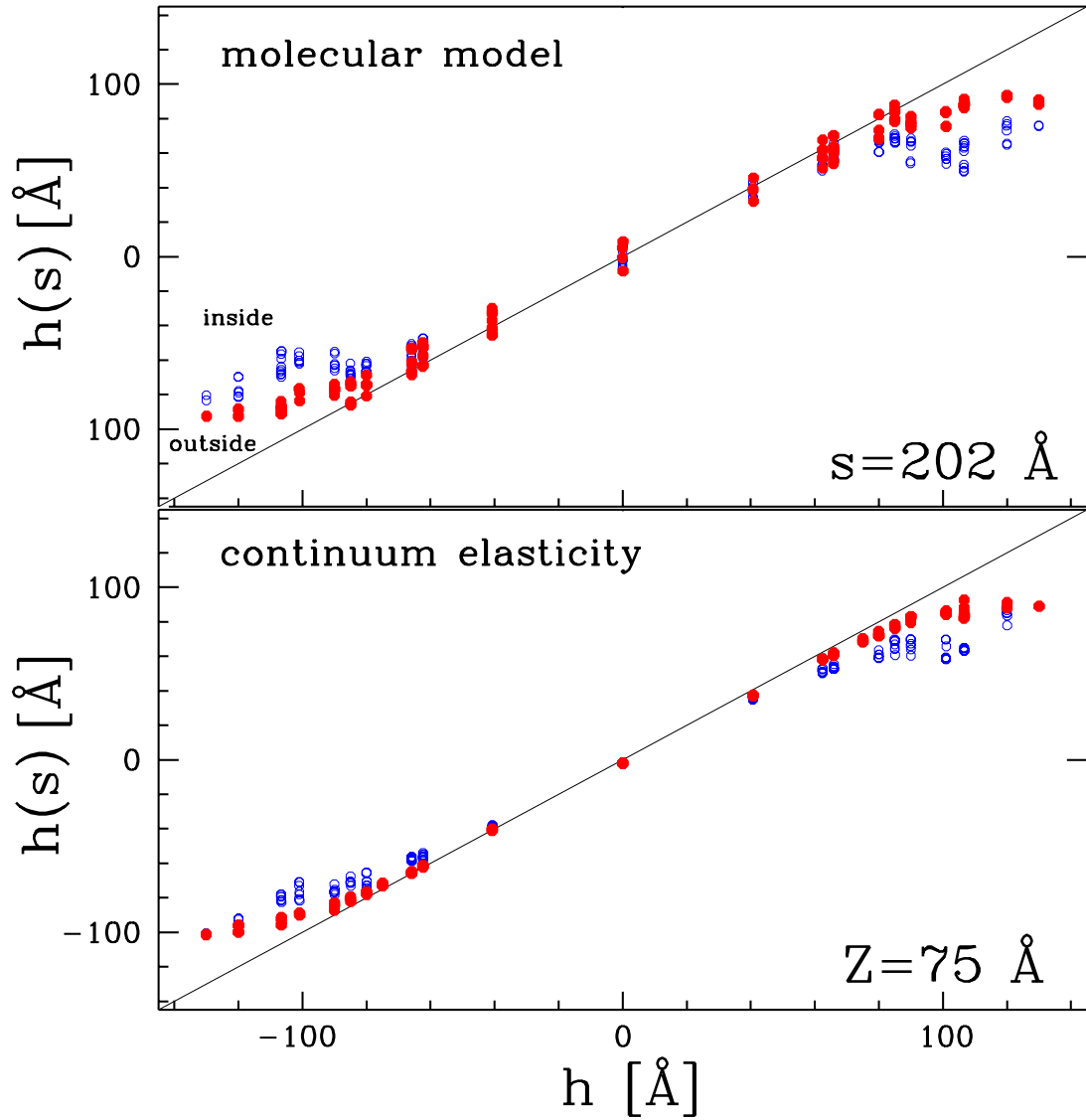


FIG. 14: Scatter plots of final vertical positions as a function of initial height for outer (solid symbols) and inner (open symbols) boundaries of the capsid. The top panel shows positions of C^α atoms for $s=202 \text{ \AA}$, and the bottom panel shows node positions from the continuum model of Gibbons and Klug at a wall displacement of $Z = 75 \text{ \AA}$. [12].

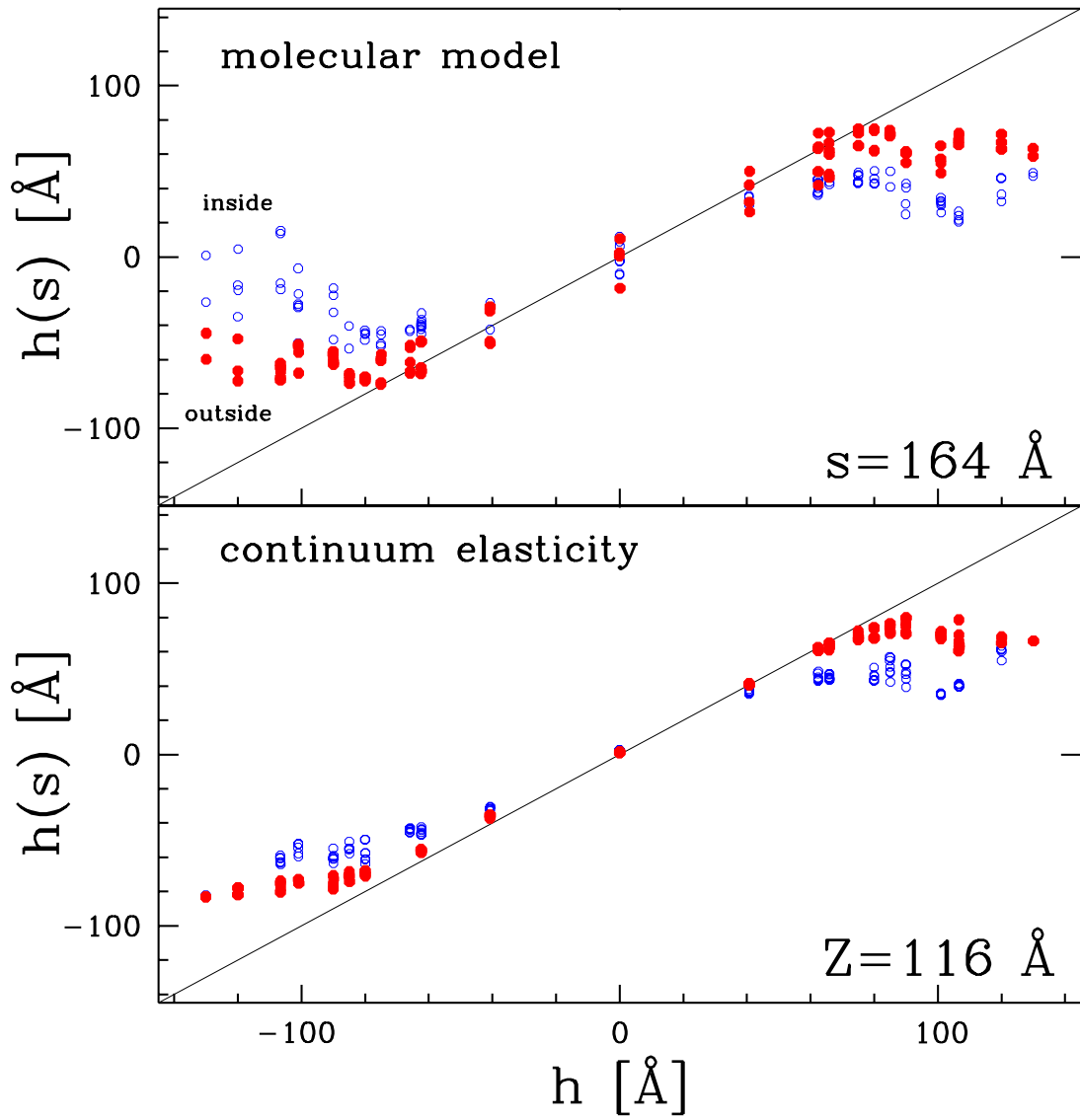


FIG. 15: Similar to Figure 14 but for a higher compression corresponding to $s=164 \text{ \AA}$.

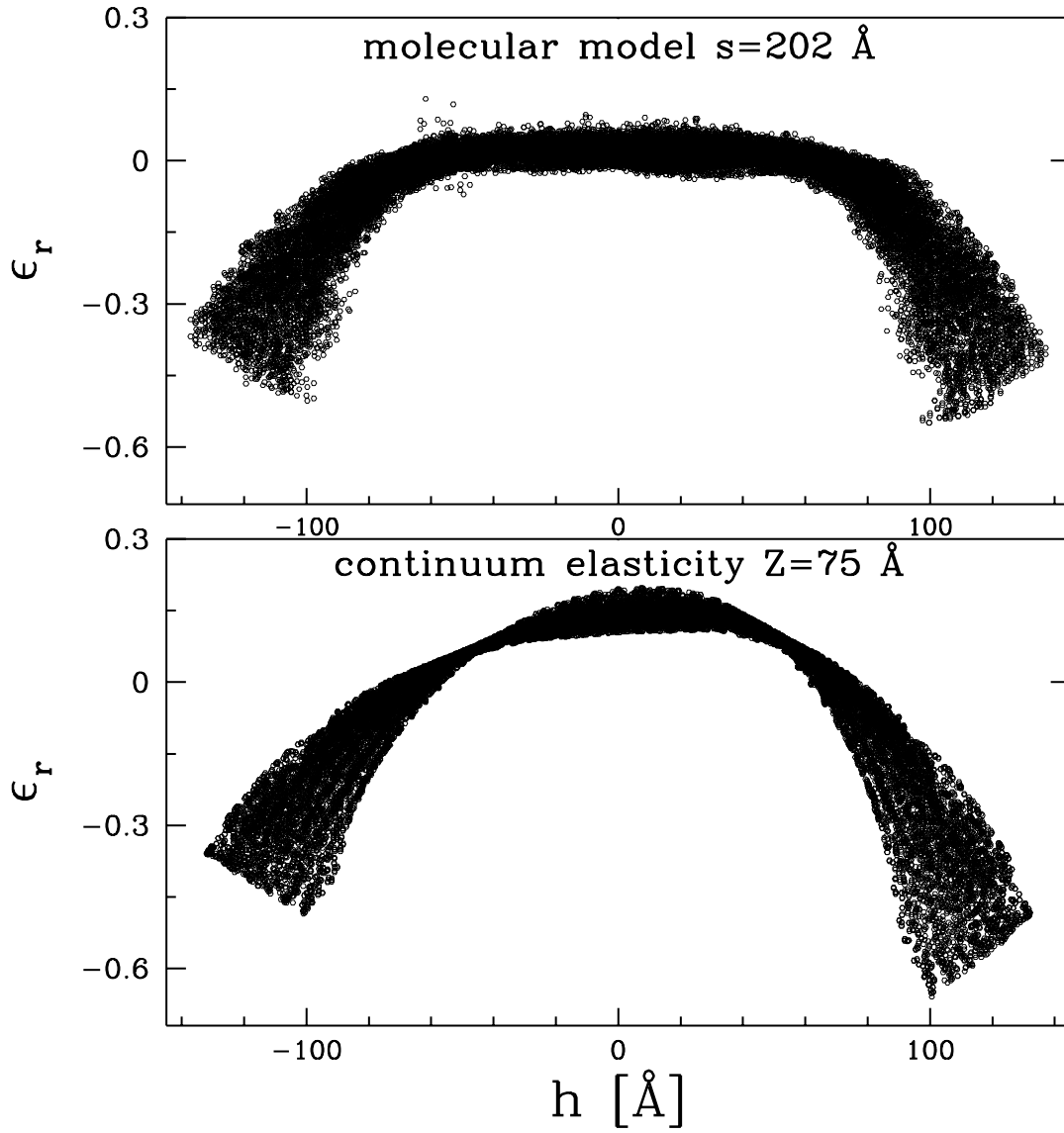


FIG. 16: Scatter plots for the radial strain as a function of height corresponding to a wall separation of $s = 202 \text{ \AA}$. The top panel is for the molecular model and the bottom from the data provided by Gibbons and Klug from a continuum model [12].

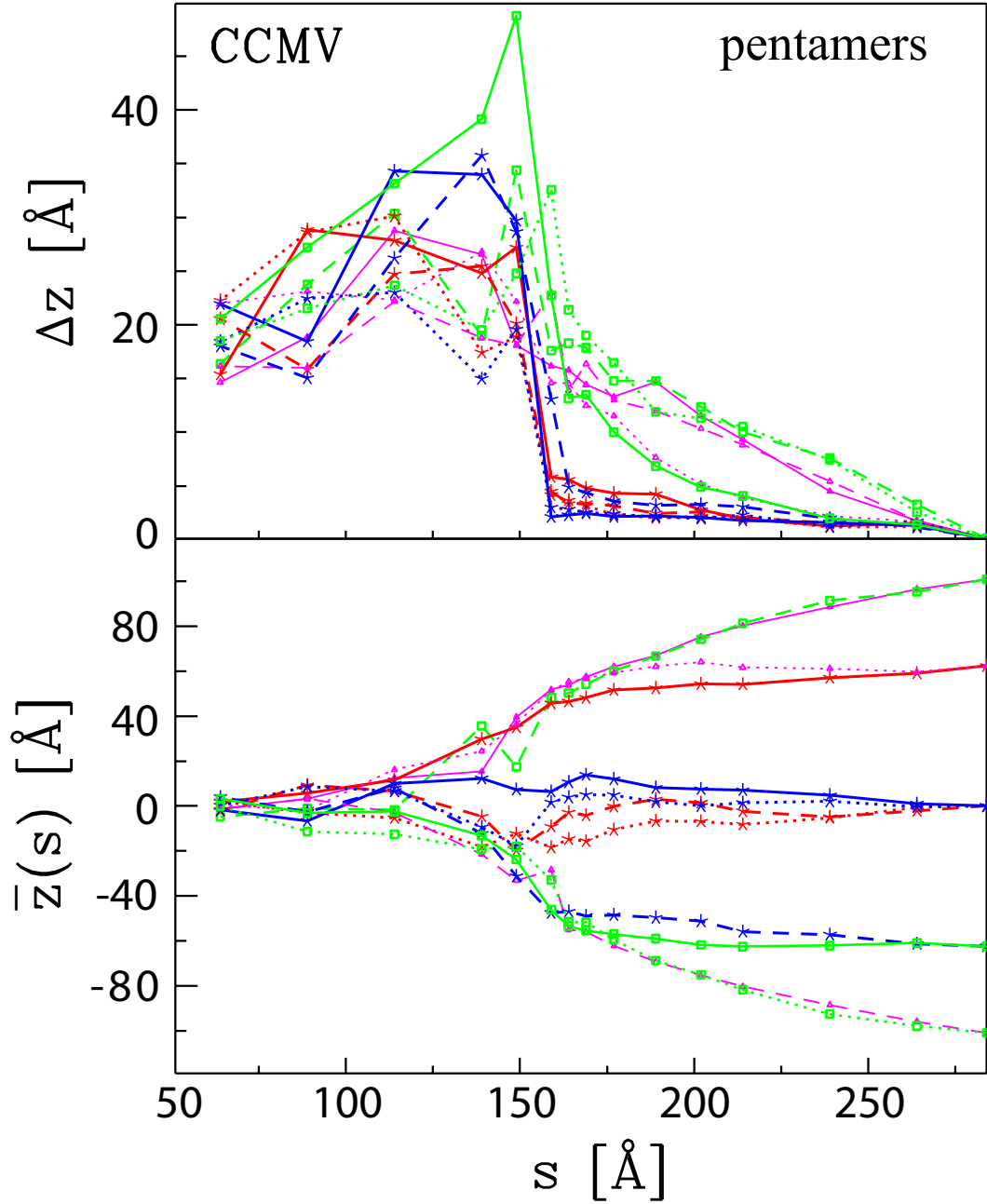


FIG. 17: The bottom panel shows the height of the centers of mass of atoms belonging to 12 individual pentamers. The top panel shows rms variation in the height change of atoms belonging to the same pentamer. The outer lines in the bottom panel correspond to the polar pentamers and the lines in the middle to the equatorial regions. The same symbols are used in the top panel.

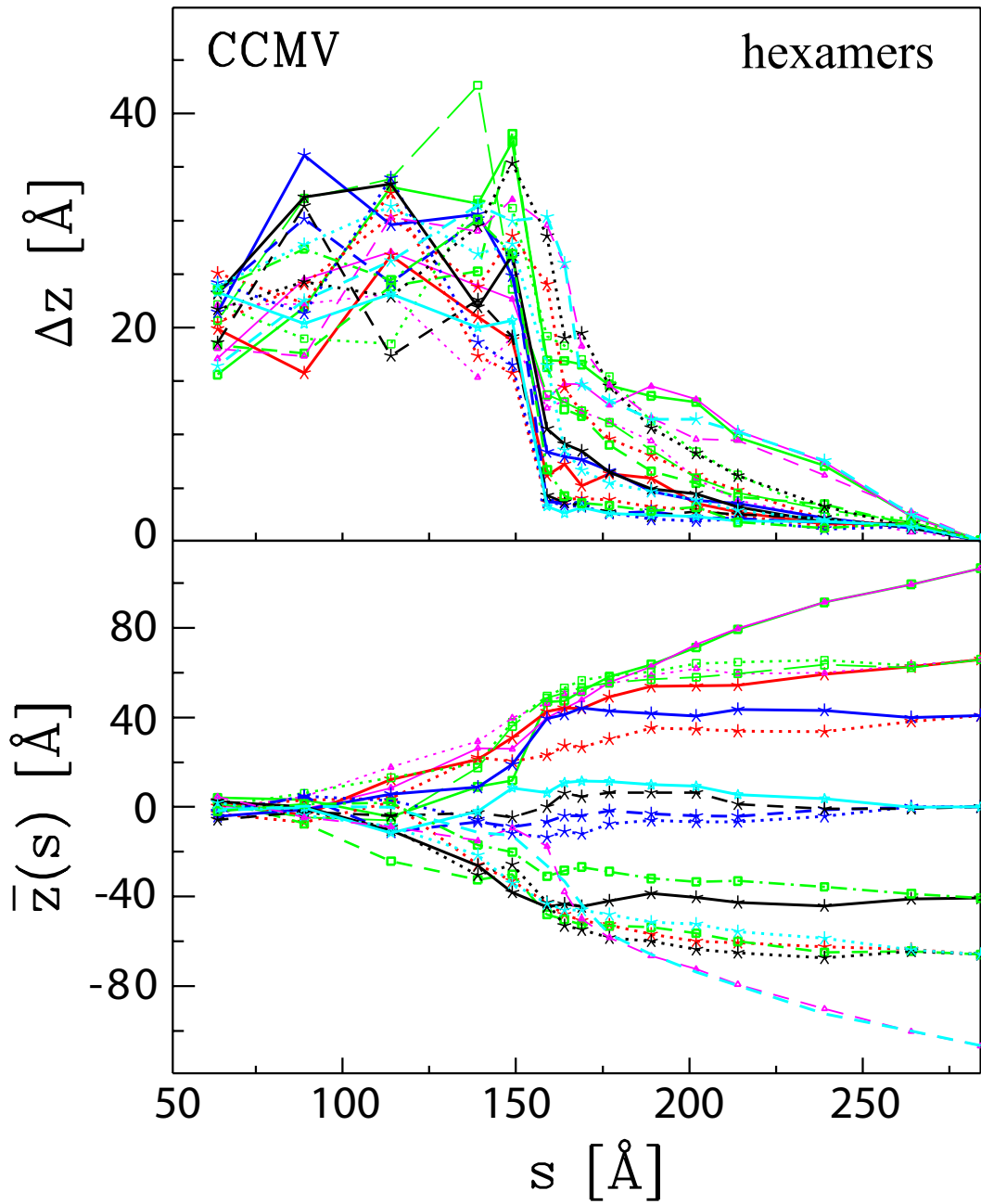


FIG. 18: Similar to Figure 17 but for the 20 hexamers.